Digitális Állampolgárként
elektronikusan aláírta:
CSIKSZENTMIHÁLYI MÁRK

MÁRK CSÍKSZENTMIHÁLYI
FINAL PROJECT

BUDAPEST UNIVERSITY OF TECHNOLOGY AND ECONOMICS
FACULTY OF MECHANICAL ENGINEERING
DEPARTMENT OF HYDRODYNAMIC SYSTEMS



FINAL PROJECTS

BUDAPEST UNIVERSITY OF TECHNOLOGY AND ECONOMICS
FACULTY OF MECHANICAL ENGINEERING
DEPARTMENT OF HYDRODYNAMIC SYSTEMS

Márk Csíkszentmihályi

Final project

Coupling of fluid mechanics and acoustics on moving geometries

Consultant:
Dr.techn. Dr.h.c. Manfred Kaltenbacher
Univ.-Professor

Supervisor:
Dr. György Paál
Univ.-Professor

Budapest, 2026

Copyright © Márk Csíkszentmihályi, 2026.

Budapest University of Technology and Economics
Faculty of Mechanical Engineering
Department of Hydrodynamic Systems
http://www.hds.bme.hu/

FINAL PROJECT ASSIGNMENT

Publicly Available

Identification

Name: **Csikszentmihályi Márk**			ID: **71615020701**
Code of the Curriculum: 2N-MW0		Specialisation: 2N-MW0-FM	Document ref. number: GEVG:2026-2:2N-MW0:QZ17DG
Curriculum: Gépészeti modellezés mesterképzési szak			
Final Project issued by: Hidrodinamikai Rendszerek Tanszék		Final exam organised by: Áramlástan Tanszék	
Supervisor: Dr. Paál György (71958119266), professor			

Project Description

Title	**Coupling of fluid mechanics and acoustics on moving geometries** Áramlástan és akusztika kapcsolása mozgó geometriák esetén
Details	1. Review the relevant literature. 2. Simulate the flow of a human larynx model with moving grid, representing vocal fold motion. 3. Adapt OpenFOAM and openCFS to enable coupling via the preCICE software. 4. Compute the acoustic source terms, using the flow field data and interpolate them onto a coarser acoustic grid. 5. Compute the acoustic field, using the same moving geometry as for the flow computation. 6. Compare the results of the different methods and simulation settings. 7. Write the thesis in concordance with the given formal and content requirements.
Advisor	Advisor's Affiliation: Insitute of Fundamentals and Theory in Electrical Engineering, Graz University of Technology AT-8010 Graz, Austria, Inffeldgasse 18 Advisor: Dr. Manfred KALTENBACHER, Head of Department

Final Exam

1st subject (group)	2nd subject (group)	3rd subject (group)	4th subject (group)
ZVEGEÁTNW02 Computational Fluid Dynamics	**ZVEGEÁTNW03** Fluid Mechanics Measurements	**ZVEGEVGNX28** Theoretical Acoustics	**ZVEGEVGNX26** Hemodynamics

Authentication

Handed out: 16 February 2026		Deadline: 29 May 2026
Compiled by: Dr. Paál György (71958119266) Supervisor	Verified by: *Dr. György Paál* (signed) Head of Department	Approved by: *Dr. Gábor Györke* (signed) Vice-Dean

The undersigned declares that all prerequisites of the Final Project have been fully accomplished. Otherwise, the present assignment for the Final Project is to be considered invalid.

……..
Csikszentmihályi Márk

DECLARATIONS

Declaration about the independent work

I, *Márk Csíkszentmihályi* (QZ17DG), hereby declare that the Thesis submitted for assessment and defence, exclusively contains the results of my own work assisted by my supervisor. Further to it, it is also stated that all other results taken from the technical literature or other sources are clearly identified and referred to according to copyright (foot-notes/references are chapter and verse, and placed appropriately).

I accept that the scientific results presented in my Thesis can be utilised by the Department of the supervisor for further research or teaching purposes.

Graz, 10^{th} June 2026

Márk Csíkszentmihályi

Contents

Preamble **IX**

Nomenclature **X**

List of figures **XIV**

1 Introduction **1**

1.1 Objectives 2

1.2 Overview 3

2 Theoretical background **4**

2.1 Physiology of voice production 4

2.1.1 Anatomy of the laryngeal region 4

2.1.2 Vocal fold vibration 5

2.1.3 Mechanical and aerodynamic parameters 7

2.2 Flow induced sound 7

2.2.1 Conservation equations for fluid dynamics 8

2.2.2 Flow and acoustics 9

2.2.3 Acoustic wave equation 10

2.2.4 Aeroacoustic properties 12

2.3 Computational Aeroacoustics 13

2.3.1 Perturbation of flow quantities 15

2.3.2 Source term interpolation 16

3 Literature review **19**

3.1 Classical aeroacoustic analogies 19

3.1.1 Lighthill's acoustic analogy 19

3.1.2 Curle's formulation 20

3.1.3 Ffowcs Williams-Hawkings equation 20

3.1.4 Vortex sound 21

3.2 Direct Numerical Simulation for CAA 21

3.3 Perturbation equations 22

3.4 Numerical modeling of human phonation 24

3.4.1 Multi-mass models 24

3.4.2 PDE based approaches . . . 25

4 CAA model of human voice production 28

4.1 Methodology . . . 28

4.2 Flow simulation . . . 29

4.2.1 Boundary conditions . . . 29

4.2.2 Mesh definition . . . 32

4.2.3 Numerics and solver settings . . . 34

4.3 Acoustic simulation on fixed grid . . . 34

4.3.1 Computational domain . . . 34

4.3.2 Boundary conditions and mesh . . . 35

4.3.3 Source term interpolation . . . 36

4.3.4 Numerics and solver settings . . . 37

4.4 Acoustic simulation on moving grid . . . 38

4.4.1 Mesh motion definition . . . 38

4.4.2 Source term calculation and interpolation . . . 38

4.4.3 Solver settings and methods . . . 39

4.5 Results . . . 40

4.5.1 Velocity fields . . . 40

4.5.2 Pressure field . . . 43

4.5.3 Wave propagation . . . 46

4.5.4 Acoustic pressure . . . 49

4.5.5 Frequency spectra . . . 50

5 Summary 52

5.1 Results . . . 52

5.2 Conclusion and outlook . . . 53

Összefoglaló 54

References 55

Preamble

Aeroacoustics studies the generation of sound by fluid flow. Human voice production represents one of its most fascinating examples, where airflow from the lungs is transformed into audible sound through the interaction of fluid dynamics, structural mechanics, and acoustics. This process lies at the intersection of engineering and medical science, making phonation a subject of interest not only for understanding human communication but also for improving the diagnosis and treatment of voice disorders.

Due to the limited accessibility of the laryngeal region, numerical modelling has become an essential tool for investigating the mechanisms of phonation. From an aeroacoustic perspective, voice production is commonly studied using a hybrid computational approach in which the flow and acoustic fields are solved separately and coupled through acoustic source terms derived from the flow solution. Nevertheless, source term interpolation and acoustic wave propagation are commonly performed on fixed acoustic meshes, despite the continuous deformation of the domain caused by vocal fold motion.

This thesis develops and implements a hybrid aeroacoustic workflow for the simulation of human voice production on moving acoustic meshes. The framework enables acoustic computations on time-varying domains, addressing a limitation of conventional hybrid approaches based on fixed acoustic meshes.

* * *

Acknowledgement

First and foremost, I would like to express my heartfelt gratitude to my family and to my fiancée, Réka, for their unwavering support. The emotional encouragement they provided was invaluable in helping me complete this thesis while spending much of my time abroad.

I would also like to express my sincere gratitude to Prof. Dr. techn. Dr. h.c. Manfred Kaltenbacher for giving me the opportunity to join the Institute of Fundamentals and Theory in Electrical Engineering at Graz University of Technology, and for his continuous guidance and support. I am especially grateful to Patrick Heidegger for his conscientious assistance and constant availability throughout this work.

Finally, I would like to thank Prof. Dr. György Paál for his support in the completion of my Final Project from the side of my home university.

Graz, 10^{th} June 2026

Márk Csíkszentmihályi

Nomenclature

The table contains the names of the notations that occur several times, and in the case of physical quantities, its unit of measurement. The designation of each quantity is, where possible, the same as that accepted in the domestic and international literature. An explanation of the rarely used notations can be found at their first location.

Latin letters

Notation	Name, comment, value	Dimension
A	displacement amplitude	m
B	constant of damper	Ns/m
c	speed of sound	m/s
d	glottal gap diameter	m
D	total derivative	
e	internal energy	J
E	Young's modulus	N/m^2
f	frequency	Hz
f_a	right-hand side force of PCWE	m/s^2
f_p	probability distribution	
$\mathbf{f}$	body force	N/m^3
$F(t)$	time-dependent force	N
h	enthalpy	m^2/s^2
H	total stagnation enthalpy	m^2/s^2
$H(f)$	Heaviside function	
$\mathbf{I_a}$	acoustic intensity	W/m^2
K	spring constant	N/m
l_{gd}	glottal duct length	m
l_{vf}	vocal fold length	m
L	characteristic length scale	m
L_c	characteristic width	m
L_{ij}	Lighthill's stress tensor	Pa
L_p	sound pressure level	dB
M	mass	kg
$\mathbf{n}$	normal vector	1
p	pressure	Pa
p	normalization exponent	
P	threshold pressure	Pa
P_a	acoustic power	W
$\mathbf{P}$	characteristic point	
q_h	heat source	W/m^3
$\mathbf{q}_T$	heat flux	W/m^2
r	radius	m
R	normalization radius	m
s	surface	m^2
t	time	s
T	period time	s

Latin letters (continued)

Notation	Name, comment, value	Dimension
$\mathbf{u}$	velocity	m/s
$\mathbf{U}$	velocity	m/s
v	velocity	m/s
v_n	n^{th} interpolated value	
w_i	weight for nearest neighbour interpolation	
w	vertical displacement	m
w_{vf}	vocal fold thickness	m
x	distance	m

Greek letters

Notation	Name, comment, value	Dimension
α	spatial weighting function	
Γ	boundary	
δ	Kronecker delta	
κ	isentropic exponent	1
λ	wavelength	m
λ_F	molecular mean free path	m
ν	kinematic viscosity	m^2/s
ρ	density	kg/m^3
σ	stress tensor	Pa
τ	viscous stress	Pa
ϕ	scalar potential	m^2/s
ϕ	phase shift	
ψ	acoustic potential	m^2/s
$\mathbf{\Psi}$	vector potential	m^2/s
$\boldsymbol{\omega}$	vorticity vector	1/s
Ω	collision operator	

Indices, exponents, acronyms

Notation	Name, comment, value
a	acoustic
h	harmonic
i	row index
j	column index
ic	incompressible
irr	irrotational
max	maximum
ref	reference
rms	root-mean-square
s	solid
th	threshold

Indices, exponents, acronyms (continued)

Notation	Name, comment, value
v	vortical
VFu	upper vocal fold
VFl	lower vocal fold
0	mean value, undisturbed state
1	correction term, first value
2	second value
$\overline{\square}$	mean value
$\square'$	fluctuating part
$\dot{\square}$	time derivative
$\ddot{\square}$	second time derivative
∂	derivative
$\mathcal{O}$	order of approximation
AI	Artificial Intelligence
APE	Acoustic Perturbation Equations
CAA	Computational Aeroacoustics
CFD	Computational Fluid Dynamics
CFL	Courant-Friedrichs-Lewy condition
CFS	Coupled Field Simulation
DNS	Direct Numerical Simulation
FEM	Finite Element Method
FFT	Fast Fourier Transform
FVM	Finite Volume Method
FW-H	Ffowcs Williams-Hawkings equation
IBM	Immersed Boundary Method
MRI	Magnetic Resonance Imaging
LBM	Lattice-Boltzmann Method
LEE	Linearized Euler Equations
LES	Large Eddy Simulation
LPCE	Linearized Perturbed Convective Equation
OVM	Overset Mesh Method
PCE	Perturbed Convective Equations
PCWE	Perturbed Convective Wave Equation
PDE	Partial Differential Equation
RHS	Right hand side
RMS	Root-mean-square
SGS	Sub-grid-scale
SPL	Sound Pressure Level

List of Figures

1.1 Mechanism of human voice production 1
2.1 Cross-section front view of the larynx and the vocal fold 4
2.2 Cartilaginous structure of the human larynx 5
2.3 Schematic representation of the vocal fold oscillation cycle 6
2.4 Decomposition of the velocity flow field 10
2.5 Acoustic pressure fluctuations during wave propagation 11
2.6 Order of magnitudes of flow and acoustic properties 14
2.7 The hybrid CAA workflow 14
2.8 Interpolation and nodal redistribution of acoustic source terms 16
2.9 Nearest neighbour interpolation technique 17
2.10 Conservative interpolation techniques 18
3.1 Acoustic source mechanisms of the Ffowcs Williams-Hawkings equation . . 21
3.2 Single mass-spring oscillatory model of the vocal folds 24
3.3 Three-dimensional multi mass-spring model of vocal folds 25
3.4 Parametrized geometry of the M5 vocal fold model 25
3.5 PCWE source terms during vocal fold oscillation 26
4.1 Boundary segments of the CFD domain 29
4.2 Characteristic points of the vocal fold prescribed motion 30
4.3 Characteristic motion phases of a vocal fold oscillation cycle 31
4.4 Meshed domain of the larynx geometry for CFD simulation 32
4.5 Skewness of the CFD mesh 33
4.6 Acoustic domain and its main computational regions 35
4.7 Meshed geometry of the computational acoustic domain 36
4.8 Comparison of CFD and acoustic meshes in the laryngeal region 37
4.9 Workflow of the acoustic simulation on moving grid 39
4.10 Velocity field at characteristic time instants for 100 Hz case 41
4.11 Velocity field at characteristic time instants for 200 Hz case 42
4.12 Pressure field at characteristic time instants for 100 Hz case 44
4.13 Pressure field at characteristic time instants for 200 Hz case 45
4.14 Acoustic potential fields at eight time instant for fixed grid case 47
4.15 Acoustic potential fields at eight time instant for moving grid case 48
4.16 Acoustic pressure for fixed and moving grids (100Hz case) 49

4.17 Acoustic pressure for fixed and moving grids (200Hz case) 50
4.18 Frequency spectrum for fixed and moving grids (100Hz case) 50
4.19 Frequency spectrum for fixed and moving grids (200Hz case) 51

1 Introduction

The human voice is one of the fundamental elements of communication. It enables us to convey information, express thoughts and emotions, connect with others, or engage in activities such as singing. At the same time, voice production (also called as phonation) is a complex process from both biological and engineering perspectives. Its scientific complexity, as well as individual and societal importance, is aptly summarized by the following quote, attributed to the renowned German composer Richard Strauss [1]:

"Human voice is the most beautiful instrument of all, but the most difficult to play."

According to a survey conducted in 2018, approximately 16% of the population experience mild, and 1.4% severe phonation-related problems [2], indicating that such conditions are relatively common. These various voice disorders are still actively investigated within the medical community, including potential surgical interventions and therapeutic approaches. However, research in this field is significantly obstructed by the limited accessibility of the laryngeal region, which restricts the feasibility of direct, so-called *in vivo* measurements [3]. Consequently, numerical simulations have gained increasing importance over the past decades, with the underlying physical fields modelled with the help of descriptive partial differential equations (PDEs).

From an engineering standpoint, phonation can be described as a highly complex, triply coupled phenomenon involving fluid dynamics, structural mechanics, and acoustics [4]. Airflow generated by a pressure gradient in the lungs is transformed into an audible signal in the larynx, as displayed in Figure 1.1. The vocal folds, located in the glottal region of the larynx, periodically oscillate under the combined influence of aerodynamic, muscular, and elastic forces [5]. During each vibration cycle, the vocal folds alternately open and close completely, producing a pulsating jet flow. This disturbed, turbulent flow field in the supraglottal region acts as the primary source of sound wave generation, making phonation an aeroacoustic phenomenon. The resulting sound is then shaped within the oral and nasal cavities, making it perceivable.

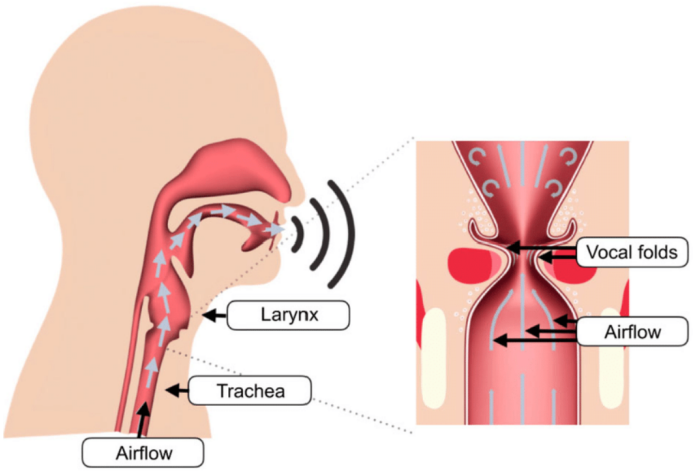


Figure 1.1: Mechanism of human voice production. Extracted from [6].

The thesis focuses on the computational aeroacoustic (CAA) aspect of voice production, specifically the modelling of sound sources arising from flow phenomena. A current state-of-the-art approach in CAA is the so-called hybrid methodology [7], where the flow and acoustic fields are solved separately and coupled through an aeroacoustic formulation. In such hybrid workflows, fluid dynamics and acoustic wave propagation are typically computed on separate computational grids, each tailored to the respective physical phenomenon to reduce computational cost. Fluid meshes require high resolution to resolve turbulent structures, whereas acoustic meshes – designed to capture acoustic wavelengths – are generally coarser. As a result, transferring data between the two grids requires an additional interpolation step. The acoustic source terms, computed on the CFD mesh, must be mapped onto the nodes of the acoustic mesh in a physically consistent manner.

1.1 Objectives

The existing literature exclusively performs the interpolation step and acoustic simulation in hybrid CAA frameworks on fixed acoustic meshes. However, a more realistic representation of the physical problem may be achieved by synchronizing the motion of the acoustic domain with the CFD simulation. This allows both the source term interpolation and acoustic wave propagation to be performed on moving acoustic nodes. The present study aims at develop and implement a hybrid aeroacoustic framework that can handle moving geometries in human voice production simulations. The study compares simulations performed on fixed and moving acoustic meshes and assesses the influence of mesh motion on the resulting acoustic field.

In the glottal region, airflow remains in the low Mach number regime, justifying the incompressible flow assumption. For acoustic wave propagation, we employ the Perturbed Convective Wave Equation (PCWE), in which the acoustic source terms are derived from the incompressible pressure field. This results in a computationally efficient hybrid modelling framework in which the source terms are transferred between the CFD and acoustic domains through interpolation. In this partitioned setup, wave propagation is computed using the finite-element (FEM) based open-source software, openCFS [8]. A key limitation of the existing workflow is that openCFS does not natively support source-term interpolation onto deforming acoustic meshes. To overcome this limitation, an external workflow is required. The acoustic mesh motion must be decomposed into discrete time steps, and the CFD solution must be interpolated onto the corresponding acoustic mesh configuration at each time instance. Representative excitation frequencies of 100 Hz and 200 Hz are considered, which correspond to typical male and female phonation ranges, respectively. To make a comprehensive comparison, simulations are performed using both the conventional configuration, which includes a moving CFD mesh and a fixed acoustic mesh, resulting in four simulation configurations overall.

Finally, the thesis aims at providing a comprehensive overview of the numerical modelling approach for human voice production, including theoretical foundations, computational workflow, and current limitations. Through this, the thesis contributes to a deeper understanding of flow-induced sound generation and its numerical representation in phonation-related aeroacoustic simulations.

1.2 Overview

Following this introduction, Chapter 2 presents the theoretical background, fundamental principles, and methods necessary to understand the present work. It covers the physiological and biomechanical aspects of human phonation and provides a general overview of aeroacoustics and its computational treatment. The chapter also introduces perturbation-based approaches and numerical coupling through data interpolation in hybrid CAA frameworks. Chapter 3 provides a literature review of the aeroacoustic analogies developed over the past few decades, along with existing scientific results related to the numerical modelling of human phonation. Chapter 4 describes the methodologies applied in this work and the practical implementation of the modelling framework. It discusses flow and acoustic simulations separately, including a detailed presentation of the workflow for the moving acoustic mesh case. Finally, Chapter 5 presents and evaluates the obtained results. The thesis concludes with a summary of the main findings, a discussion of potential future research directions, and a Hungarian-language summary.

2 Theoretical background

2.1 Physiology of voice production

Since phonation characteristics are fundamentally linked to human anatomy, the biological aspects of the phenomenon are discussed before its aeroacoustic modelling. The anatomy of the larynx, including the vocal folds within it and the downstream vocal tract, fundamentally determines the path and character of the airflow originating from the lungs. The vocal folds exhibit a highly distinctive periodical motion that is only partially driven by intrinsic muscles. Rather, the continuous airflow itself acts as the primary sustaining mechanism for these self-excited oscillations, which can exceed hundreds cycles per second. A solid understanding of the key physical parameters is indispensable for the subsequent modelling steps because they provide the basis for defining appropriate boundary conditions, material properties, and physically justified simplifications.

2.1.1 Anatomy of the laryngeal region

The larynx is a cartilaginous organ located in the neck, with an approximate length of 4-5 cm. The laryngeal airway can be divided into three main regions along its longitudinal direction: the subglottal region is located below the vocal folds, the glottal region contains the vocal folds, and the supraglottal region is located above the vocal folds. This triple division is illustrated in Figure 2.1a.

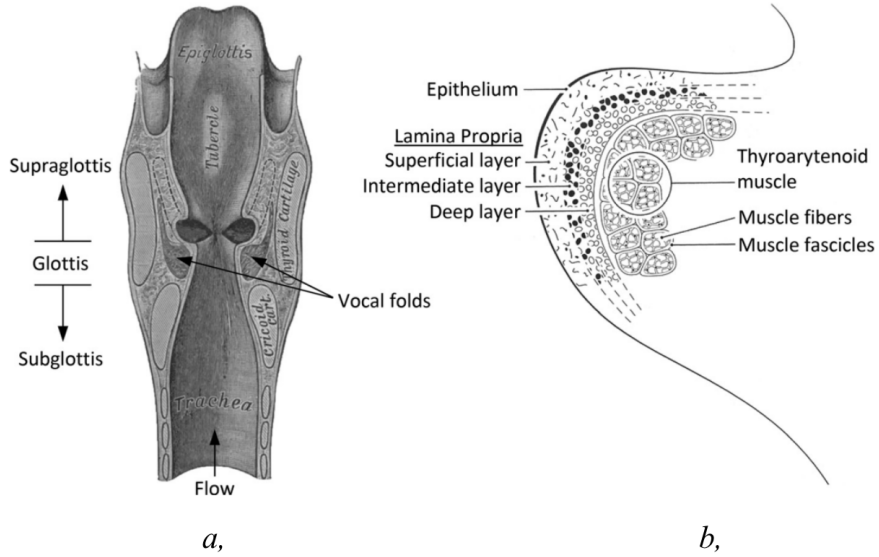


Figure 2.1: (a) Cross-section view of the larynx (b) Inner layered structure of the vocal fold. Extracted from [9], originally from [10, 11].

The larynx is composed of hard and soft tissues. The hard tissue consists of four major cartilages: the epiglottis, thyroid, cricoid, and arytenoid (displayed in Figure 2.2). The hyoid bone, located at the upper end of the larynx, maintains an open space for airflow. The soft tissue contains two vocal folds that are symmetrically opposed and undergo periodic oscillatory motion under the action of airflow. In addition to the vocal folds, the

larynx also contains the ventricular (false) folds that do not actively participate in the oscillatory process of phonation. From a structural point of view, the vocal folds build up from the mucosa and a deeper, vocalise muscle (see Figure 2.1b). The outer surface of the mucosa is formed by the epithelium, a thin protective layer with a thickness of approximately $50\mu m$. Beneath the epithelium lies the lamina propria, which is commonly divided into three sublayers: superficial, intermediate, and deep. Together, the epithelium and the superficial layer of the lamina propria form the cover, which plays a major role in the natural, self-sustained oscillatory motion due to its fluid-like, elastic structure [12]. The inner part of the vocal folds, often referred to as the body, consists of the thyroarytenoid muscle, and is responsible for vocal fold activation and tension controls during human speech.

The characteristic length of the vocal folds typically ranges from 10 to 20 mm, depending mainly on sex [6].

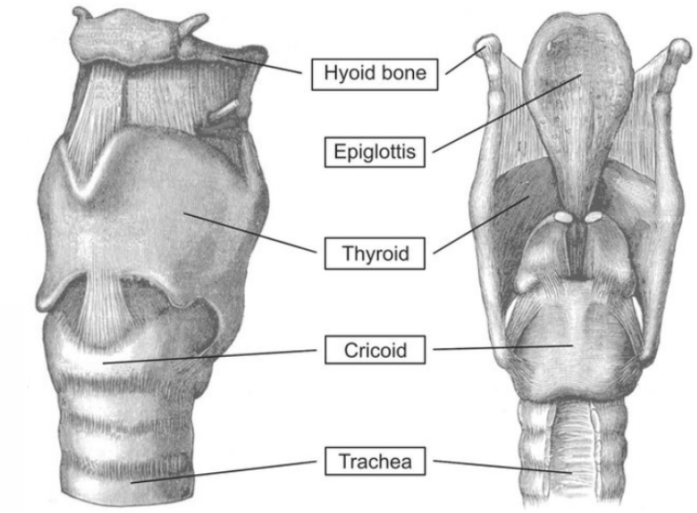


Figure 2.2: Cartilaginous structure of the hard tissue of the human larynx. Modified from [3], originally from [10].

2.1.2 Vocal fold vibration

The periodic oscillation of the vocal folds is primarily driven by the airflow generated by the pressure difference between the lungs and the outside environment. During phonation, air from the lungs travels through the trachea, passes the larynx, and exits through the vocal tract into the ambient air. To initiate vocal fold oscillation, the subglottal pressure must exceed a minimum threshold, which for humans is typically in the range of 100–300 Pa [13]. The vocal folds vibrate passively, meaning that their oscillatory motion is not directly generated by muscular actuation, but rather by the interaction between the airflow and the viscoelastic tissue structure of the folds [14]. Once oscillation begins, the coupled fluid–structure interaction becomes self-sustained, with aerodynamic forces continuously transferring energy to the tissue motion.

Advances in Magnetic Resonance Imaging (MRI) now make it possible to non-invasively reconstruct three-dimensional, time-resolved representations of vocal fold vibration (e.g. [15]). During an oscillation cycle, the vocal folds periodically modify the glottal geometry by alternating between convergent and divergent configurations (see Figure 2.3). This propagating deformation pattern is commonly referred to as the mucosal wave [16]. Under healthy conditions, the vocal folds touch during each oscillation cycle, temporarily closing the glottal gap.

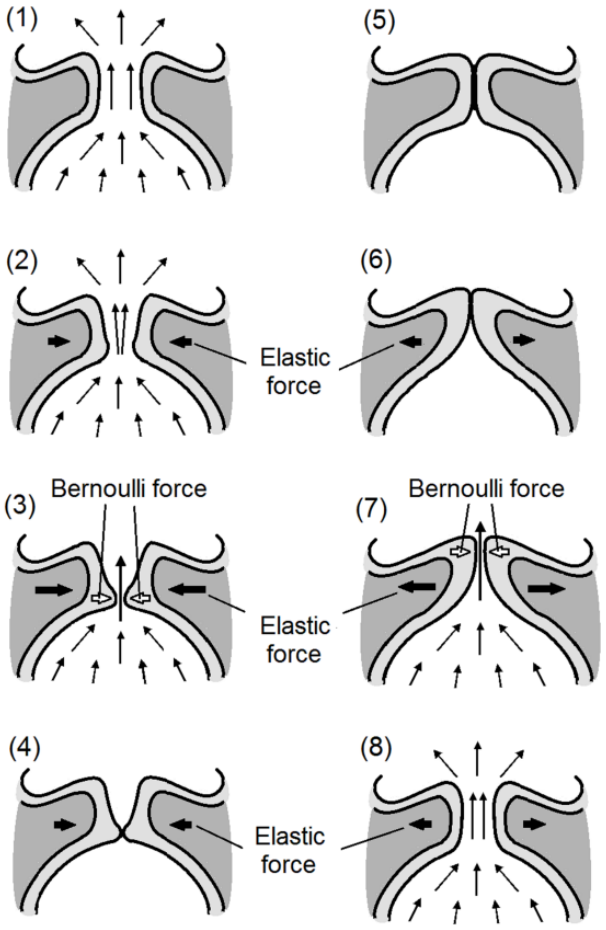


Figure 2.3: Schematic representation of the vocal fold oscillation cycle. Extracted from [17].

The oscillatory motion of the vocal folds generates an unsteady, pulsating jet in the supraglottal region. As the flow passes through the narrow glottal constriction, vortical structures develop downstream of the glottis. These unsteady flow features induce pressure fluctuations that act as the primary aeroacoustic sources of voice production. The resulting acoustic waves then propagate through the vocal tract, where the oral and nasal cavities further shape and filter the sound. This determines the perceived characteristics of the voice.

2.1.3 Mechanical and aerodynamic parameters

During human speech, the vocal folds oscillate at a frequency of about 100 Hz to 200 Hz. This requires mechanical properties that combine sufficient stiffness with proper flexibility. The typical geometric, aerodynamic and material parameters of the vocal folds and the laryngeal region are summarized in Table 2.1.

Table 2.1: Typical geometric, aerodynamic, and material parameters of the human vocal folds and glottal flow. Adapted from [3].

Parameter	**Value**
Vocal fold length (anterior–posterior)	$l_{vf} = 10{-}17$ mm
Vocal fold thickness (inferior–superior)	$w_{vf} = 9{-}10$ mm
Glottal gap diameter	$d = 0{-}5$ mm
Glottal duct length	$l_{gd} = 2{-}5$ mm
Subglottal oscillation threshold pressure	$P_{\text{th}} = 200{-}1000$ Pa
Maximum intraglottal velocity	$U_{\max} = 10{-}40$ m/s
Fundamental frequency	$f = 80{-}300$ Hz
Reynolds number	$Re = \dfrac{U_{\max} d}{\nu} = \mathcal{O}(10^3)$
Mach number	$Ma = \dfrac{U_{\max}}{c} = \mathcal{O}(10^{-1})$
Strouhal number	$St = \dfrac{f d}{U_{\max}} = \mathcal{O}(10^{-2})$
Average vocal fold Young's modulus	$E = 5{-}20$ kPa

2.2 Flow induced sound

Voice production is governed by the principles of flow-induced sound generation, also known as aeroacoustics. Interacting with the vocal folds and the surrounding geometry, the airflow gives rise to unsteady flow structures that act as sound sources.

A consistent mathematical description requires the combination of fluid dynamics and acoustics within a unified framework. This includes the fundamental equations of fluid mechanics, velocity field decomposition according to Helmholtz, and the identification of acoustic phenomena based on the irrotational part of the flow. The physical connection between fluid motion and acoustics can be described in terms of the isotropically expanding component of the irrotational velocity field. The acoustic wave equation is formulated to describe the propagation of pressure disturbances using either acoustic pressure or, indirectly, acoustic potential representations.

2.2.1 Conservation equations for fluid dynamics

The change in the physical properties of any flow can be expressed mathematically by conservation equations. The conservation equations are defined for three different properties – mass, momentum and energy – and establish relationships among the flow field variables. In this case, fluid is treated as a continuum, meaning all molecules within a given control domain have the same field variable values [18].

Conservation of mass states that no mass appears or disappears within a closed system. This concept is generally expressed by the relation

$$\frac{\partial \rho}{\partial t} + \nabla \cdot (\rho \mathbf{u}) = 0, \tag{2.1}$$

also known as the continuity equation. In the case of an incompressible fluid, where ρ is constant, the flow field becomes divergence-free and (2.1) simplifies to

$$\nabla \cdot \mathbf{u}_{\text{ic}} = 0. \tag{2.2}$$

Conservation of momentum originates from Newton's second law and the idea that the total momentum change is directly proportional to the sum of the forces acting on a fluid element. This relation forms the well-known Navier-Stokes equations

$$\rho \frac{D\mathbf{u}}{Dt} = -\nabla p + \nabla \cdot [\boldsymbol{\tau}] + \mathbf{f}. \tag{2.3}$$

The right-hand side (RHS) values of the equation represent force densities, i.e., pressure, viscous and volume forces, respectively. In (2.3), $\frac{D}{Dt}$ represents the substantial derivative, which – for an arbitrary quantity of $f(t, \mathbf{x})$ – is defined as

$$\frac{Df}{Dt} = \frac{\partial f}{\partial t} + (\mathbf{u} \cdot \nabla) f \tag{2.4}$$

in an Euelerian frame.

Due to the conservation of energy, the total change of the energy density is balanced as

$$\rho \frac{D\left(\frac{u^2}{2} + e\right)}{Dt} = q_h - \nabla \cdot \mathbf{q}_T - \nabla \cdot (p\mathbf{u}) + \nabla \cdot ([\boldsymbol{\tau}] \cdot \mathbf{u}) + \mathbf{f} \cdot \mathbf{u}, \tag{2.5}$$

with e being the inner energy, q_h the heat source and $\mathbf{q}_T$ the heat flux. The third, fourth and fifth terms on the RHS represent energies coming from surface pressure force, surface shear force and force density, respectively [19].

The continuity equation, the Navier-Stokes equations and the energy equation form a set of PDEs that describe the flow. However, the number of equations is still less, than of the unknowns, which is bridged by the so-called constitutive relations. In the context of aeroacoustics, the relevant auxiliary laws [20] are the Newtonian fluid relation, which connects velocity with the stress tensor, and the state equation for pressure, given by

$$dp = c^2 d\rho. \tag{2.6}$$

2.2.2 Flow and acoustics

Helmholtz's decomposition establishes the conceptual connection between flow and acoustics. According to this theorem, any velocity field can be expressed as the sum of an irrotational and a vortical component:

$$\mathbf{u} = \underbrace{\nabla\phi}_{\mathbf{u}_{\mathrm{irr}}} + \underbrace{\nabla \times \boldsymbol{\Psi}}_{\mathbf{u}_{\mathrm{v}}}, \tag{2.7}$$

where ϕ is the scalar potential and $\boldsymbol{\Psi}$ is the vector potential.

For incompressible flows, the absence of vortical structures (i.e. $\nabla \times \boldsymbol{\Psi}^{\mathrm{ic}} = 0$) yields curl- and divergence-free potential flow. When vorticity is also present, the potential flow is supplemented by the vortical part $\mathbf{u}_{\mathrm{v}}$. Vorticity is defined as the curl of the velocity field and is therefore associated only with the vortical component as

$$\boldsymbol{\omega} = \nabla \times \nabla \times \boldsymbol{\Psi}^{\mathrm{ic}} = \nabla \times \mathbf{u}_{\mathrm{v}}^{\mathrm{ic}}. \tag{2.8}$$

To investigate compressible flows, the decomposed velocity field (2.7) can be inserted into a rewritten form of the continuity equation (2.1), which yields

$$\frac{1}{\rho}\frac{D\rho}{Dt} = -\nabla \cdot \nabla\phi - \nabla \cdot \nabla \times \boldsymbol{\Psi} = -\nabla \cdot \nabla\phi. \tag{2.9}$$

In (2.9), the divergence of the vortical component vanishes identically, meaning that density variations are solely governed by the scalar potential through its Laplacian. Compressibility, a crucial requirement for acoustic wave propagation, is thus entirely linked to the irrotational component of the velocity field. The vortical component does not contribute to sound propagation.

This implies that the full velocity field can be decomposed into an orthogonal triple, where the irrotational part is divided into a harmonic part and a compressible part, in addition to the vortical structure $\mathbf{u}_{\mathrm{v}}$ as

$$\mathbf{u} = \mathbf{u}_{\mathrm{v}} + \mathbf{u}_{\mathrm{irr}}^{\mathrm{h}} + \mathbf{u}_{\mathrm{irr}}^{\mathrm{c}} = \nabla \times \boldsymbol{\Psi} + \nabla\phi^{\mathrm{h}} + \nabla\phi^{\mathrm{c}}. \tag{2.10}$$

In (2.10), $\nabla\phi^{\mathrm{h}}$ represents the harmonic subpart, which describes the potential flow. The other irrotational term $\nabla\phi^{\mathrm{c}}$ is responsible for the unsteady, compressible structure and is the sole origin of the acoustic field [21].

This decomposition is consistent with Batchelor's interpretation of fluid motion, as described in his work [22]. Batchelor showed that the velocity field of a continuum point can be represented as a superposition of three fundamental types of motion: isotropic expansion, pure straining motion and rigid-body rotation (see Figure 2.4). Since sound is generated by local density fluctuations, isotropic expansion, which involves a change in volume and therefore represents the compressible effects, reflects the fundamental mechanism of flow-originated acoustic waves.

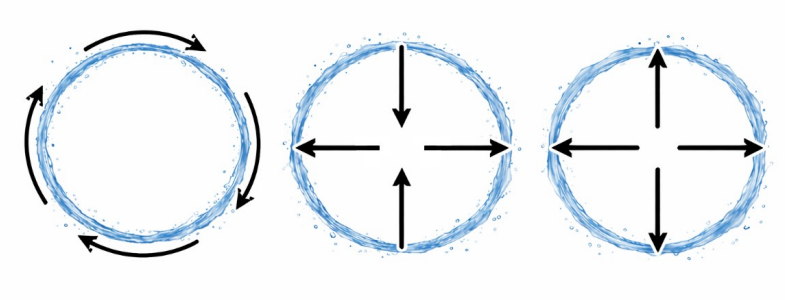


Figure 2.4: Decomposition of the flow field: rigid-body rotation (left), irrotational deformation (middle) and isotropic expansion (right). Modified from [20].

2.2.3 Acoustic wave equation

The description of sound propagation in fluids is based on the assumption that acoustic phenomena can be interpreted as small deviations (perturbations) from a steady flow state. This approximation is generally valid for low-amplitude waves, forming the basis of linear acoustics.

In this case, the primary flow variables are decomposed into mean and fluctuating (acoustic) components as

$$p = p_0 + p_\mathrm{a}, \tag{2.11}$$
$$\rho = \rho_0 + \rho_\mathrm{a}, \tag{2.12}$$
$$\mathbf{u} = \mathbf{u}_0 + \mathbf{u}_\mathrm{a}. \tag{2.13}$$

For linear acoustics to be valid, the fluctuations must be small compared to the mean values, i.e.

$$|p_\mathrm{a}| \ll p_0, \tag{2.14}$$
$$|\rho_\mathrm{a}| \ll \rho_0. \tag{2.15}$$

In many relevant cases, the mean flow can be assumed to be quiescent, such that $\mathbf{u}_0 = \mathbf{0}$ and the velocity field is entirely described by its acoustic component:

$$\mathbf{u} = \mathbf{u}_\mathrm{a}. \tag{2.16}$$

To close the system, an isentropic relationship between pressure and density is assumed. Linearizing this relation yields direct proportionality between the fluctuations,

$$p_\mathrm{a} = c_0^2 \rho_\mathrm{a}, \tag{2.17}$$

where c_0 denotes the speed of sound in the undisturbed medium.

The evolution of these small disturbances can be interpreted both in terms of temporal pressure fluctuations and spatial wave propagation. A conceptual illustration of this behavior is shown in Figure 2.5.

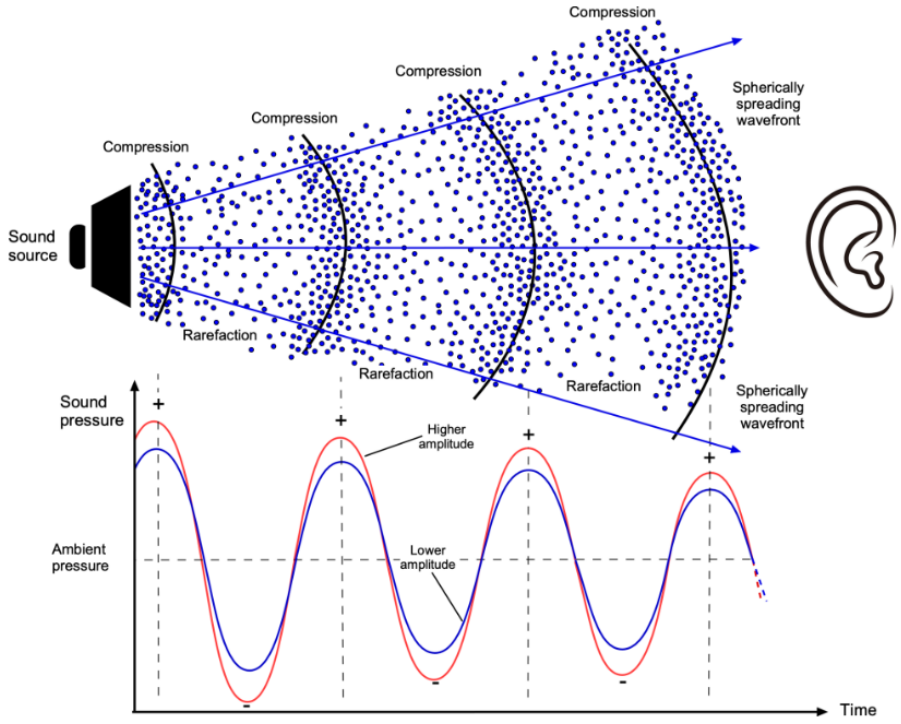


Figure 2.5: Acoustic pressure fluctuations around a mean pressure level during wave propagation. Extracted from [23].

Substituting the decomposed variables into the governing conservation equations (2.1) and (2.3) and neglecting nonlinear terms leads to the linearized conservation equations of acoustics

$$\frac{\partial \rho_\mathrm{a}}{\partial t} + \rho_0 \nabla \cdot \mathbf{u}_\mathrm{a} = 0 \tag{2.18}$$

$$\rho_0 \frac{\partial \mathbf{u}_\mathrm{a}}{\partial t} + \nabla p_\mathrm{a} = \mathbf{0}. \tag{2.19}$$

These equations describe the temporal evolution of small disturbances and form the basis of acoustic wave theory. Combining them to eliminate the velocity field yields the classical wave equation for acoustic pressure,

$$\frac{1}{c_0^2} \frac{\partial^2 p_\mathrm{a}}{\partial t^2} - \Delta p_\mathrm{a} = 0. \tag{2.20}$$

Taking the curl of the linearized momentum equation (2.19) yields zero, implying that the acoustic velocity field is irrotational. Therefore, it may be expressed in terms of an acoustic scalar potential as

$$\mathbf{u}_\mathrm{a} = -\nabla\psi_\mathrm{a}. \tag{2.21}$$

This representation is consistent with the Helmholtz decomposition introduced in Section 2.2.2, where the acoustic contribution is associated only with the irrotational component of the velocity field. Substituting (2.21) into (2.18) and (2.19) results in an equivalent wave equation for the acoustic potential:

$$\frac{1}{c_0^2}\frac{\partial^2\psi_\mathrm{a}}{\partial t^2} - \Delta\psi_\mathrm{a} = 0. \tag{2.22}$$

2.2.4 Aeroacoustic properties

This subsection introduces key flow-related and acoustic quantities to characterize aeroacoustic phenomena. The dimensionless numbers and parameters defined here are used to describe flow regimes, sound generation, and wave propagation in phonation and aeroacoustic simulations.

The Knudsen number indicates whether a fluid can be treated as a continuum or whether molecular effects must be considered explicitly. When it is several orders of magnitude smaller than one, continuum-based fluid models are valid. The Knudsen number is defined as

$$Kn = \frac{\lambda_F}{L}, \tag{2.23}$$

where λ_F denotes the molecular mean free path and L is a characteristic length scale of the flow.

The Reynolds number is used to represent the ratio of inertial and viscous forces as

$$Re = \frac{vL}{\nu}, \tag{2.24}$$

where v is the characteristic velocity, L is the characteristic length scale of the flow, and ν is the kinematic viscosity.

The Mach number describes the flow velocity relative to the speed of sound in the medium and is defined as

$$Ma = \frac{v}{c}. \tag{2.25}$$

The Mach number is used to classify flows according to their compressibility effects. In fluid flow simulations, flows with $Ma < 0.3$ can be treated as incompressible.

The acoustic wavelength, λ, defines the spatial extent of a harmonic wave and is related to frequency by

$$\lambda = \frac{c_0}{f}. \tag{2.26}$$

The RMS (root-mean-square) pressure is used to quantify the amplitude of acoustic fluctuations because it provides a time-averaged measure of the acoustic signal strength. It is defined as

$$p_{\mathrm{a,rms}} = \sqrt{\frac{1}{T}\int_{t_0}^{t_0+T} p_{\mathrm{a}}^2\, dt}, \tag{2.27}$$

where T is the period time, and $p_a = (p - p_0)$ denotes the acoustic pressure.

Sound pressure level (SPL) is defined on a logarithmic scale

$$L_{p_{\mathrm{a}}} = 20 \log_{10}\left(\frac{p_{\mathrm{a,rms}}}{p_{\mathrm{a,ref}}}\right), \tag{2.28}$$

with $p_{\mathrm{a,ref}} = 20\ \mu Pa$ representing the reference pressure corresponding to the lower threshold of human hearing. The logarithmic scaling reflects the large dynamic range of acoustic pressures.

In addition to amplitude-based measures, the transport of acoustic energy is described by the acoustic intensity

$$\mathbf{I_a} = p_{\mathrm{a}}\mathbf{u}_{\mathrm{a}}, \tag{2.29}$$

where $\mathbf{u}_{\mathrm{a}}$ is the particle velocity associated with the acoustic motion. Physically, it represents the instantaneous energy flux carried by the sound wave.

Integrating the acoustic intensity provides a global measure of the emitted acoustic power radiated through a surface. The acoustic power can be obtained as

$$P_{\mathrm{a}} = \oint_{\Gamma} \mathbf{I_a} \cdot d\mathbf{s} = \oint_{\Gamma} \mathbf{I_a} \cdot \mathbf{n}\, ds. \tag{2.30}$$

2.3 Computational Aeroacoustics

In aeroacoustics, there is a significant disparity in spatial and temporal scales between flow structures and acoustic wavelengths, as shown in Figure 2.6. For low Mach number flows, the acoustic wavelength λ is typically several orders of magnitude larger than the characteristic length scales of turbulent structures l [24], with an approximate ratio of

$$\lambda \sim \frac{l}{Ma}. \tag{2.31}$$

Due to this scale separation, fluid dynamic and acoustic simulations are generally performed separately. The acoustic source terms, derived from the flow solution, provide the coupling between the two simulations. This method is also called hybrid CAA.

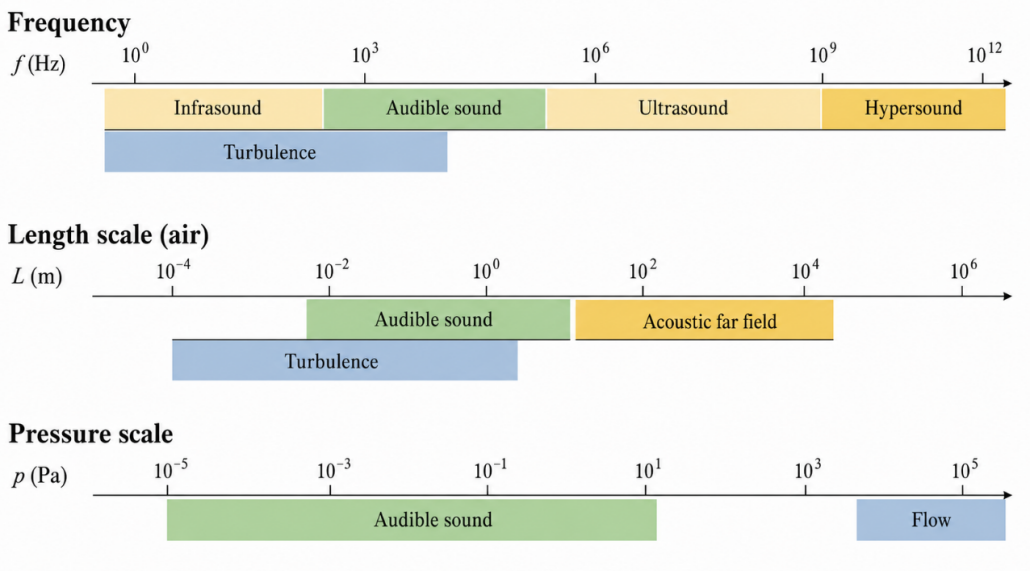


Figure 2.6: Order of magnitudes of flow and acoustic properties. Modified from [21].

Figure 2.7 illustrates the complete hybrid CAA workflow consisting of three independent steps, as described in [25]. First, the flow field is obtained from either numerical simulations or measurements. Next, acoustic source terms are computed and transferred onto the acoustic grid. Then, the radiated sound field is predicted using an aeroacoustic analogy. One widely used and computationally efficient formulation for this purpose is the PCWE [26], in which the sole unknown variable is the acoustic potential. For low Mach number flows, the corresponding source term can conveniently be obtained as the time derivative of the pressure field from an incompressible CFD simulation, scaled by the speed of sound and the constant density of the medium.

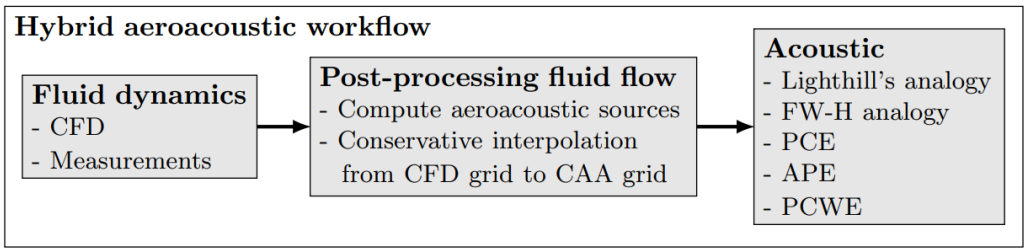


Figure 2.7: The hybrid CAA workflow. Extracted from [25].

2.3.1 Perturbation of flow quantities

Based on the separation of vortical and irrotational motion and the linear acoustic framework, the PCWE provides a formulation that explicitly links flow-induced incompressible fluctuations to acoustic wave propagation. This formulation is used to compute wave propagation in the present thesis, for which a more detailed derivation is therefore given below.

The starting point is decomposing the flow variables into a mean component and a fluctuating part, also known as the *perturbation ansatz*. For velocity and pressure, this yields

$$\mathbf{u} = \bar{\mathbf{u}} + \mathbf{u}' \tag{2.32}$$

$$p = \bar{p} + p'. \tag{2.33}$$

Unlike the purely acoustic decomposition introduced in Section 2.2.3, the fluctuating quantities are now further separated into incompressible and compressible contributions. Based on the Helmholtz decomposition, the fluctuating velocity field can be written as

$$\mathbf{u}' = \mathbf{u}_{\mathrm{ic}} + \mathbf{u}_{\mathrm{a}}, \tag{2.34}$$

so the total velocity field becomes

$$\mathbf{u} = \bar{\mathbf{u}} + \mathbf{u}_{\mathrm{ic}} + \mathbf{u}_{\mathrm{a}}. \tag{2.35}$$

Here, u_{ic} represents the vortical component associated with flow structures, and u_{a} denotes the irrotational component responsible for acoustic motion. Similarly, the scalar pressure field is approximated as

$$p = \bar{p} + p_{\mathrm{ic}} + p_{\mathrm{a}}. \tag{2.36}$$

Substituting (2.35) and (2.36) into the full compressible conservation equations and applying assumptions appropriate for low Mach number flows leads to the Acoustic Perturbation Equations (APE)

$$\frac{\partial p_{\mathrm{a}}}{\partial t} + \bar{\mathbf{u}} \cdot \nabla p_{\mathrm{a}} + \rho_0 c_0^2 \nabla \cdot \mathbf{u}_{\mathrm{a}} = -\frac{\partial p_{\mathrm{ic}}}{\partial t} - \bar{\mathbf{u}} \cdot \nabla p_{\mathrm{ic}}, \tag{2.37}$$

$$\rho_0 \frac{\partial \mathbf{u}_a}{\partial t} + \rho_0 \nabla \left(\bar{\mathbf{u}} \cdot \mathbf{u}_a \right) + \nabla p_a = 0. \tag{2.38}$$

The APE formulation consists of a coupled system of a linearized continuity and linearized momentum equations for the acoustic pressure p_{a} and acoustic particle velocity $\mathbf{u}_{\mathrm{a}}$. The source term is given by the substantial derivative of the incompressible pressure field. However, solving this coupled system is numerically and computationally demanding.

To further simplify the formulation, the irrotational nature of the acoustic velocity field is exploited. Thus the acoustic particle velocity can be expressed in terms of a scalar

acoustic potential ψ_a,

$$\mathbf{u}_a = -\nabla\psi_a. \tag{2.39}$$

Inserting (2.39) into (2.38), acoustic pressure is then directly related to the temporal and convective variations of the acoustic potential,

$$p_a = \rho_0 \frac{D\psi_a}{Dt}. \tag{2.40}$$

Finally, substituting (2.40) into (2.37) and rearranging it into a wave equation form yields the PCWE,

$$\frac{1}{c_0^2}\frac{D^2\psi_a}{Dt^2} - \nabla^2\psi_a = -\frac{1}{\rho_0 c_0^2}\frac{Dp_{ic}}{Dt}. \tag{2.41}$$

The PCWE reduces the problem to a single scalar equation for the acoustic potential, while retaining the essential physics of sound generation and propagation in low Mach number flows. The source term is the substantial derivative of the incompressible pressure field, which provides a computationally efficient alternative to the original coupled APE system.

2.3.2 Source term interpolation

In aeroacoustic simulations, the flow field is typically computed on a fine, non-uniform mesh, while the acoustic field is solved using a coarser, more regular mesh. This requires an intermediate step in which the aeroacoustic source terms, derived from the CFD solution, are interpolated from the flow mesh onto the acoustic mesh. This procedure is illustrated in Figure 2.8.

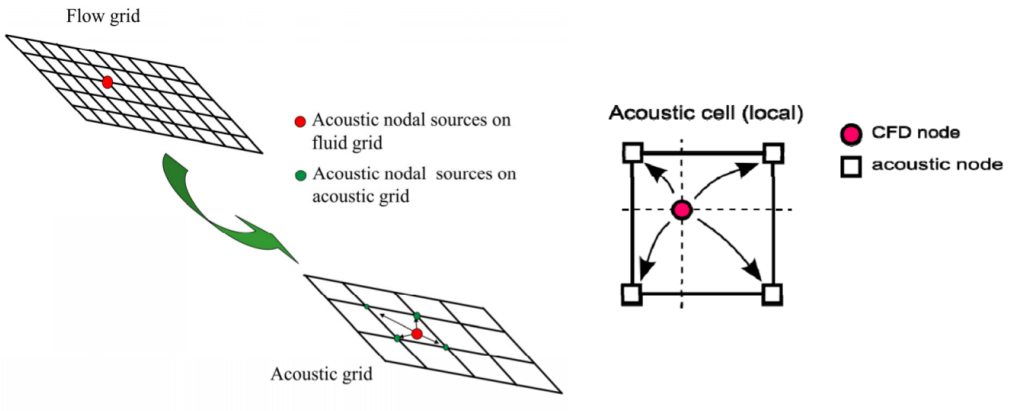


Figure 2.8: Interpolation and nodal redistribution of acoustic source terms. Modified from [27].

In this thesis, the acoustic source term is determined by the PCWE. For low Mach number flows, convective contributions can be neglected, and the source term reduces to the time derivative of the incompressible pressure field. This results in the acoustic RHS force being

$$f_{\mathrm{a}} = -\frac{1}{\rho_0 c_0^2}\frac{\partial p^{\mathrm{ic}}}{\partial t}. \tag{2.42}$$

Transferring the source terms from the CFD mesh to the acoustic mesh directly affects the accuracy of wave propagation and is therefore an important step in any hybrid aeroacoustic simulation. Different interpolation strategies have been developed based on geometry type, mesh element size, and desired accuracy.

The nearest neighbour interpolation technique [28], represented in Figure 2.9, assigns to each target node the value of the closest source element or node.

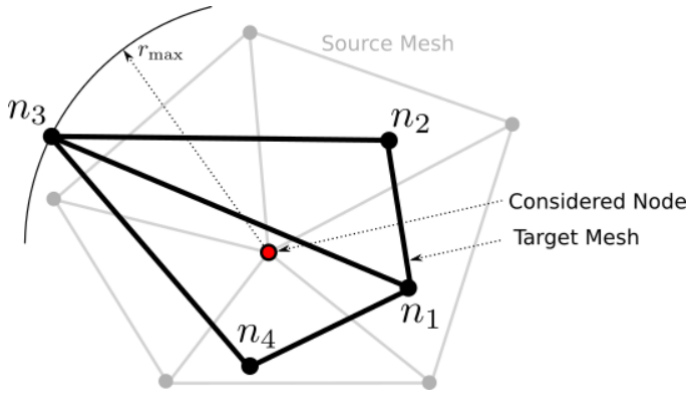


Figure 2.9: Nearest neighbour interpolation technique. Extracted from [28].

In such a case, an inverse distance weighting formula is used. For each target node, the nearest source nodes (n) are identified and their distances (r_i) to the target node are computed. The contribution of each source node is determined by the weight

$$w_i = \left(\frac{R_{\max} - r_i}{R_{\max} r_i}\right)^p, \tag{2.43}$$

where $R_{\max} = 1.01 r_{\max}$ and p is the interpolation exponent. As a result, nearby source nodes contribute more strongly to the interpolated value than more distant ones.

The interpolated value v_n at the target node is then obtained as the normalized weighted average of the neighbouring source values v_i,

$$v_n = \sum_{i=1}^{n} \frac{w_i v_i}{\sum_{i=1}^{n} w_i}. \tag{2.44}$$

Although the nearest neighbour-based method is computationally efficient and robust, it does not preserve integral quantities and may introduce errors.

More advanced, conservative methods aim to preserve the integral properties of the source term during transfer. In cell-centroid interpolation (see Figure 2.10a), the source term is first integrated over the CFD control volumes and then distributed to the acoustic finite element nodes using shape functions [29]. A more accurate variant is the cut-cell method (see Figure 2.10b), which computes the exact intersection volumes between CFD cells and acoustic elements and weights the transfer accordingly. This improves conservation for highly non-conforming meshes.

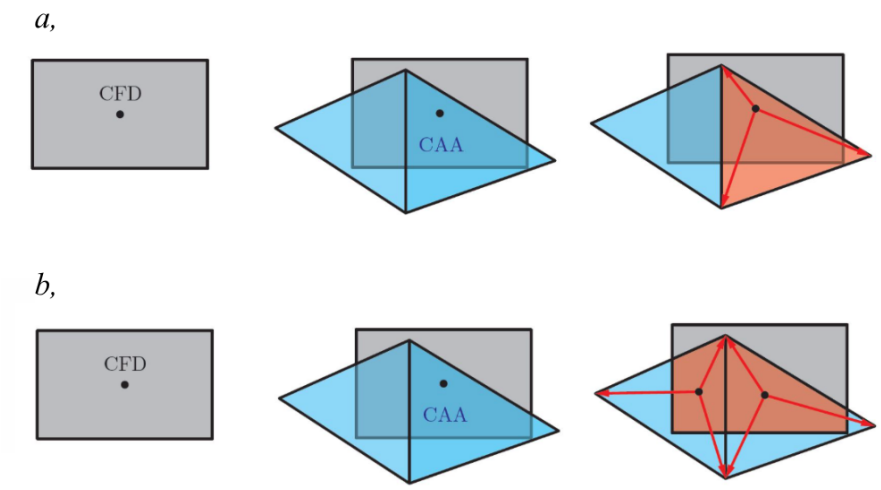


Figure 2.10: Conservative interpolation techniques: (a) cell-centroid method and (b) cut-cell method. Modified from [29].

3 Literature review

Since the early 1950s, research in aeroacoustics has yielded significant results. After Sir James Lighthill first introduced his well-known analogy [30], a variety of theoretical models were developed. As computational methods emerged and advanced, the focus shifted toward numerically solving these models.

This chapter presents the fundamental theories and models of aeroacoustics and their computational possibilities, based on the classification of Zheng *et al.* [31]. First, the principles and underlying assumptions of the classic analogies are reviewed. Next, I introduce DNS, which resolves the entire flow field without turbulence modeling and captures all relevant temporal and spatial scales of turbulence. Perturbation equation approaches are also discussed, where the base flow and acoustic variables are treated separately, introducing a more efficient way of aeroacoustic modelling.

Additionally, the milestones and scientific achievements regarding the numerical modeling of human phonation are reviewed. Early models were based on lumped-parameter representations of vocal fold dynamics using simplified mechanical analogies. More advanced approaches use continuum-based descriptions with PDEs, which allow for a more detailed description of the airflow, tissue motion and acoustic wave propagation.

3.1 Classical aeroacoustic analogies

3.1.1 Lighthill's acoustic analogy

The formal birth of aeroacoustics is marked by the work of James Lighthill [30], in which he rearranged the complete equations of compressible fluid dynamics into an inhomogeneous wave equation. Lighthill identified turbulence as the primary mechanism of noise generation [32], leading to the appearance of fluid stresses. A key element of this formulation is the Lighthill stress tensor, which represents the acoustic source term arising from turbulent flow. The stress tensor is composed of different stress components present in a general flow as

$$L_{ij} = \rho v_i v_j + \Big((p - p_0) - c_0^2(\rho - \rho_0)\Big)\,\delta_{ij} - \tau_{ij}. \tag{3.1}$$

In (3.1), the term $\rho v_i v_j$ represents the Reynolds stress, the middle term $(p-p_0)-c_0^2(\rho-\rho_0)\delta_{ij}$ is the so-called exess term and τ_{ij} is the viscous stress tensor.

For low Mach number flows ($Ma < 0.3$), the leading term is the Reynolds stress; thus, Lighthill's stress tensor can be reduced to

$$L_{ij} = \rho v_i v_j. \tag{3.2}$$

Lighthill's wave equation is then expressed as

$$\left(\frac{1}{c_0^2}\frac{\partial^2}{\partial t^2} - \nabla\cdot\nabla\right)\left(c_0^2\left(\rho - \rho_0\right)\right) = \frac{\partial^2 L_{ij}}{\partial x_i \partial x_j}. \tag{3.3}$$

In free space, the double spatial derivative of the stress tensor behaves as a quadrupole source. Since the source term is derived solely from fluid equations, a hybrid aeroacoustic approach is used, which involves computing the source terms with CFD results and performing the acoustic simulation with (3.3).

3.1.2 Curle's formulation

A few years later, Nicholas Curle [33] refined Lighthill's analogy by including the effect of solid surfaces. This was an essential step towards solving real engineering problems. Using the formal solution of the wave equation via Green's functions, Curle demonstrated that the interaction between the flow and a solid boundary introduces a new source term. In this case, the sound radiation originates from the unsteady forces (pressure and friction) acting on the surface. Mathematically, this manifests itself as a dipole source, which generates noise more efficiently than quadrupole turbulence sources do at low Mach numbers. Curle's formulation is written as

$$\begin{aligned}\left(\frac{1}{c_0^2}\frac{\partial^2}{\partial t^2} - \nabla\cdot\nabla\right)\left(c_0^2\left(\rho-\rho_0\right)H(f)\right) = &\frac{\partial^2 L_{ij}H(f)}{\partial x_i \partial x_j} \\ &- \frac{\partial}{\partial x_i}\left(\left(\rho v_i v_j + \left(p-p_0\right)\delta_{ij} - \tau_{ij}\right)\frac{\partial H(f)}{\partial x_j}\right) \\ &+ \frac{\partial}{\partial t}\left(\rho v_j \frac{\partial H(f)}{\partial x_j}\right),\end{aligned} \tag{3.4}$$

with $H(f)$ being the Heaviside function with the argument of

$$f(x) = \begin{cases} 0, & \textit{if} \quad x < 0 \\ 1, & \textit{if} \quad x \geq 0. \end{cases} \tag{3.5}$$

In (3.5), $x = 0$ defines the boundary of the solid surface Γ_s.

3.1.3 Ffowcs Williams-Hawkings equation

In 1969, John Eirwyn Ffowcs Williams and David L. Hawkings [34] extended further Curle's theory by introducing a control surface that could move arbitrarily. Thus, their equation addressed the complexities of rotating machinery, such as helicopter rotors and fans. Using the Heaviside function $H(f)$ and the Dirac delta function $\delta(f)$ enables the governing equations to be expressed for control surfaces undergoing arbitrary motion.

The Ffowcs Williams-Hawkings (FW-H) equation identifies three distinct source mechanisms, as illustrated in Figure 3.1. Monopole sources are caused by the displacement of fluid by the volume of the moving body. Dipole sources originate from the unsteady pressure distribution on the surface, and quadrupole sources are caused by turbulent stresses in the surrounding fluid.

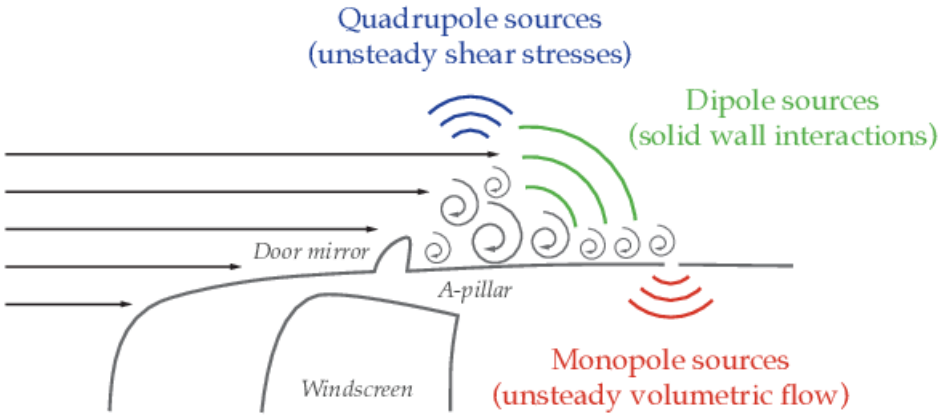


Figure 3.1: Acoustic source mechanisms in the Ffowcs Williams-Hawkings equation. Extracted from [35].

3.1.4 Vortex sound

M. S. Howe [36] reinterpreted sound generation when introduced his vortex sound theory. His derivation of the vortex sound equation for homentropic flows begins with Crocco's form of the momentum equation and, after neglecting entropy and thermal effects, yields

$$\frac{D}{Dt}\frac{1}{c_0^2}\frac{DH}{Dt} + \frac{1}{c_0^2}\frac{D\mathbf{u}}{Dt}\cdot\nabla H - \Delta H = \nabla\cdot(\boldsymbol{\omega}\times\mathbf{u}) - \frac{1}{c_0^2}\frac{D\mathbf{u}}{Dt}\cdot(\boldsymbol{\omega}\times\mathbf{u})\,. \tag{3.6}$$

In (3.6), the dominant sources are vorticity and entropy inhomogeneities [7], while

$$H = h + \frac{\mathbf{u}^2}{2} \tag{3.7}$$

represents the total stagnating enthalpy and the term $\boldsymbol{\omega}\times\mathbf{u}$ is called the Lamb vector. For low Mach numbers, linearization leads to the convective wave equation [37]

$$\left(\frac{1}{c_0^2}\frac{D^2}{Dt} - \nabla\cdot\nabla\right) H = \nabla\cdot(\boldsymbol{\omega}\times\mathbf{u})\,, \tag{3.8}$$

which is a more convenient formulation.

3.2 Direct Numerical Simulation for CAA

Direct numerical simulation is a fundamental technique in CAA, although it is generally restricted to low-Reynolds-number flows [38]. DNS solves the compressible Navier-Stokes equations without turbulence modeling, thereby naturally capturing sound generation because it simultaneously resolves both the flow and acoustic fields. However, turbulence contains a wide range of small-scale structures that require extremely fine spatial and

temporal discretization, resulting in a high computational cost. Consequently, DNS is primarily used for simple configurations in the high Mach number regime. Although the available literature is relatively limited, the theory behind it maintains the relevance of related scientific research. The most significant contributions in this area are reviewed below.

Colonius [39] investigated how sound is generated due to vortex pairing in a compressible mixing layer using DNS. He demonstrated that common simplifications in acoustic source modelling can lead to significant inaccuracies. In the context of cavity flows, Gloerfelt [40] compared results obtained from DNS with those computed using the FW-H method, as well as with experimental results. Similarly, Marsden [41] demonstrated the application of high-fidelity simulations to flow control by using Large Eddy Simulation (LES) to study active noise control in a three-dimensional cavity flow. Beck and Munz [42] discussed the challenges of direct noise computation, such as the need to accurately resolve turbulent flow structures and acoustic waves, and proposed a high-order Discontinuous Galerkin framework.

The Lattice-Boltzmann Method (LBM), introduced by Succi [43], became an efficient alternative approach to DNS for fluid flows. It simplifies the nonlinear differential equations that describe macroscopic fluid dynamics [44] using the Boltzmann equation

$$\frac{Df_p}{Dt} = \frac{\partial f_p(t, \mathbf{x}, \mathbf{u})}{\partial t} + u\frac{\partial f_p(t, \mathbf{x}, \mathbf{u})}{\partial x} = \Omega, \tag{3.9}$$

with f_p being the probability distribution function, $\mathbf{u}$ the velocity and Ω the collision operator. The method is widely used for turbulent flows [45][46], and in industrial applications [47] as well.

3.3 Perturbation equations

The concept of perturbation equations in CAA was first introduced by Hardin and Pope [48], who developed the viscous/acoustic splitting technique. In their formulation, the compressible flow variables are decomposed into an incompressible base flow and a perturbation component. To ensure that the resulting field behaves isentropically [49], a density correction term ρ_1 is included, resulting in

$$\mathbf{u} = \mathbf{u}_{\text{ic}} + \mathbf{u}' \tag{3.10}$$
$$p = p_{\text{ic}} + p' \tag{3.11}$$
$$\rho = \rho_{\text{ic}} + \rho_1 + \rho'. \tag{3.12}$$

This expansion on the incompressible flow laid the foundation for many subsequent developments. Shen and Sørensen [50] extended the method to non-isentropic flows, while Seo and Moon [51] introduced the Perturbed Compressible Equations (PCE), which account for near-field coupling between vortical and acoustic components. For efficient low Mach number aeroacoustic simulations, they introduced a linearized form (LPCE) [52] as

$$\frac{\partial \rho'}{\partial t} + \mathbf{u}_{\mathrm{ic}} \cdot \nabla \rho' + \rho_{\mathrm{ic}} \nabla \cdot \mathbf{u}' = 0 \tag{3.13}$$

$$\frac{\partial \mathbf{u}'}{\partial t} + \nabla \left(\mathbf{u}_{\mathrm{ic}} \cdot \mathbf{u}' \right) + \frac{1}{\rho_{\mathrm{ic}}} \nabla p' = \mathbf{0} \tag{3.14}$$

$$\frac{\partial p'}{\partial t} + \mathbf{u}_{\mathrm{ic}} \cdot \nabla p' + \kappa p_{\mathrm{ic}} \nabla \cdot \mathbf{u}' + \mathbf{u}' \cdot \nabla p_{\mathrm{ic}} = -\frac{dp_{\mathrm{ic}}}{dt} \tag{3.15}$$

to ensure stability and grid independency.

In parallel, the Linearized Euler Equations (LEE) were developed by linearizing the Euler equations around a mean flow [20]:

$$\frac{\partial \rho'}{\partial t} + \bar{\mathbf{u}} \cdot \nabla \rho' + \mathbf{u}' \cdot \nabla \bar{\rho} + \bar{\rho} \nabla \cdot \mathbf{u}' + \rho' \nabla \cdot \bar{\mathbf{u}} = 0 \tag{3.16}$$

$$\frac{\partial \mathbf{u}'}{\partial t} + \bar{\mathbf{u}} \cdot \nabla \mathbf{u}' + \mathbf{u}' \cdot \nabla \bar{\mathbf{u}} + \frac{1}{\bar{\rho}} \nabla p' - \frac{1}{\bar{\rho}^2} \nabla \left(p' \bar{p} \right) = \mathbf{0} \tag{3.17}$$

$$\frac{\partial p'}{\partial t} + \bar{\mathbf{u}} \cdot \nabla p' + \mathbf{u}' \cdot \nabla \bar{p} + \kappa \bar{p} \nabla \cdot \mathbf{u}' + \kappa p' \nabla \cdot \bar{\mathbf{u}} = 0. \tag{3.18}$$

Although widely used, modifications were required to ensure purely acoustic wave propagation. A major advancement in this direction was achieved with the Acoustic Perturbation Equations (APE), formulated by Ewert and Schröder [53]. These equations introduce a decomposition into mean, vortical, and acoustic components as

$$\mathbf{u} = \bar{\mathbf{u}} + \mathbf{u}' = \bar{\mathbf{u}} + \mathbf{u}_{\mathrm{v}} + \mathbf{u}_{\mathrm{a}}, \tag{3.19}$$

combined with source-term filtering to isolate acoustically relevant contributions. Several variants (APE-1, APE-2, APE-3 and APE-4) exist, differing mainly in source modeling and variable formulation.

A further simplification is provided by the Perturbed Convective Wave Equation, which can be interpreted as an exact reformulation of the APE-2 system under low Mach number assumptions and with the neglect of entropy and vortical mode coupling [37]. This reduces the governing system to a single scalar equation for the acoustic potential, resulting in a computationally efficient formulation:

$$\frac{1}{c_0^2} \frac{D^2 \psi_{\mathrm{a}}}{Dt^2} - \nabla \cdot \nabla \psi_{\mathrm{a}} = -\frac{1}{\rho_0 c_0^2} \frac{D p_{\mathrm{ic}}}{Dt}. \tag{3.20}$$

This equation is derived and discussed in more detail in Section 2.3.1.

3.4 Numerical modeling of human phonation

3.4.1 Multi-mass models

Due to the anatomical inaccessibility of the laryngeal region, measurement-based investigations are restricted. For this reason, researchers have developed computational models of phonation dating back to the 1960s. Over time, these models have progressed from simplified, low-dimensional systems to detailed, PDE-based formulations. [54].

Computational modelling began with multi-mass models, which were designed to capture the core oscillatory mechanics of the vocal folds. In general, these reduced-order models are a simplification of real motion and allow only large-scale investigations [55]. Flanagan and Landgraf [56] first introduced a single mass-spring oscillatory model to represent self-sustained vocal fold vibrations.

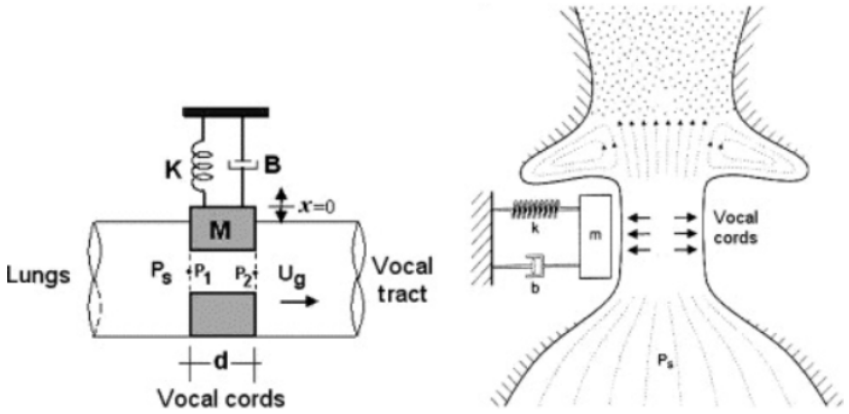


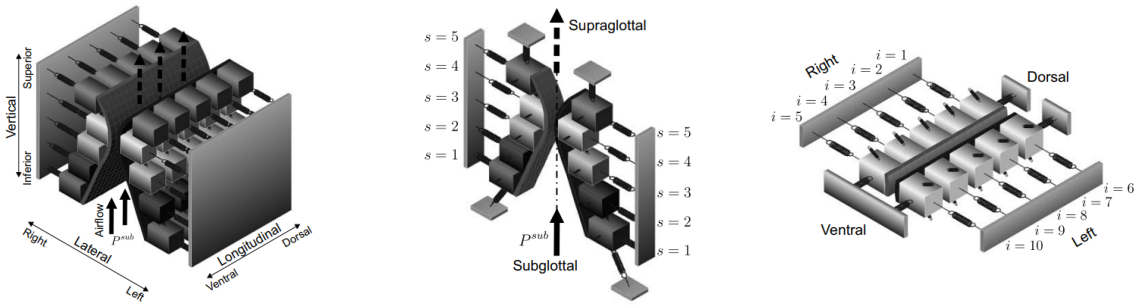
Figure 3.2: Single mass-spring oscillatory model of the vocal folds. Extracted from [57].

The system is driven by a time-dependent force $F(t)$, generated by air pressure and distributed over the intraglottal surface, with its resultant acting on mass M [57]. This system is illustrated in Figure 3.2, where the dynamics of the vocal folds is given by

$$M\ddot{x} + B\dot{x} + Kx = F(t), \tag{3.21}$$

where M is the mass, K is the constant of the spring and B is the constant of the damper.

The single mass-spring model was then followed by more refined representations. Ishizaka and Flanagan [58] introduced a two-mass model, which allows one to describe the phase shift between the upper and lower vocal folds and thus approximate wave-like motions more accurately. Story and Titze's three-mass model [59] incorporated a physiologically motivated body–cover structure with adjustable muscle-related parameters. This resulted in a more realistic simulation of vertical phase differences. Titze introduced a mucosal wave model [60], in which he defined a surface-type wave perpendicular to the airflow. Yang *et al.* [61] developed a three-dimensional mass–spring cover model that extends prior low-dimensional approaches by capturing full three-dimensional vocal fold dynamics across the medial surface. This model represents the vocal folds as multiple vertically stacked layers of longitudinally coupled oscillators (see Figure 3.3).



(a) **(b)** **(c)**

Figure 3.3: Multi-mass-spring vocal fold model: (a) full three-dimensional view, (b) vertical cross-section, and (c) horizontal cross-section. Extracted from [61].

3.4.2 PDE based approaches

Starting in the 2000s, early studies began applying PDE-based formulations to simulate phonation with increasing physical realism and complexity. Alipour *et al.* [62] described vocal fold vibration using two-dimensional finite elements for the basic continuum mechanical model. Rosa *et al.* [63] contributed to the topic by performing a coupled 3D simulation with a coarse mesh setup. They successfully reproduced the key vibratory features and demonstrated the influence of the false vocal folds on the laryngeal behavior. Meanwhile, Scherer *et al.* [64] introduced a geometric representation of the vocal folds (Figure 3.4), known as the M5 model, which has since been widely used. The main advantage of the model is the parametric control of the glottal contour, which allows for systematic variation of vocal fold shapes.

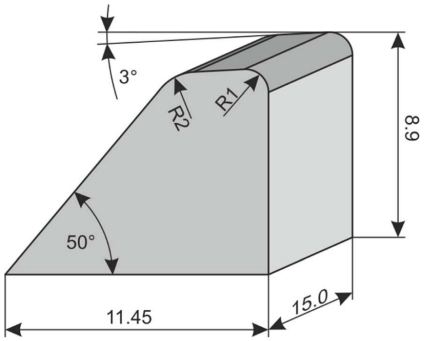


Figure 3.4: Parametrized geometry of the M5 vocal fold model. Extracted from [55].

Flow field simulations of the glottal region began to emerge when Mihaescu [65] used LES to characterize the formation of intra-glottal vortices in a divergent glottis, thereby demonstrating how vortices arise under steady inflow. Mattheus [66] took into account the movement of the vocal folds for the first time, when compared two- and three-dimensional setups regarding glottal jet flow. Zheng *et al.* [67] used the Immersed Boundary Method (IBM) to handle the numerical mesh for movement, while others used the Overset Mesh Method (OVM), e.g. in [68].

Beyond CFD simulations, several studies have also computed acoustic propagation using different modeling approaches. Zörner *et al.* [69] demonstrated how different glottal geometries and oscillation patterns influence flow behavior and thus acoustic source generation, using APE. Based on the same splitting-based APE, Šidlof *et al.* compared convergent and divergent glottal configurations [70] and also demonstrated that the simulated acoustic spectra agree well with measured formant frequencies. They validated the approach for investigating flow–sound interactions in voice production, presented in [71].

However, only a limited number of such studies exist, DNS-based simulations have also been applied. One example is the work of Schickhofer *et al.* [72], who computed acoustic radiation for different vowels using fully compressible CFD. Thus, fluid–acoustic interactions were directly captured, but at the cost of higher computational effort.

Schoder *et al.* [29] introduced the application of PCWE to human phonation. They showed that optimized interpolation and grid reduction can decrease computational costs by up to 95%, while maintaining satisfactory acoustic accuracy. In [25], they demonstrated that the time derivative of pressure contributes more significantly to the overall far-field sound spectrum and demonstrated that neglecting convective terms introduces only minimal error. The publication contains many visualizations in both the frequency and time domains, separately for the convective term, the pressure time derivative, and the full source term combining the two. In Figure 3.5, these combined source term values are presented for different phases of the vocal fold oscillation cycle.

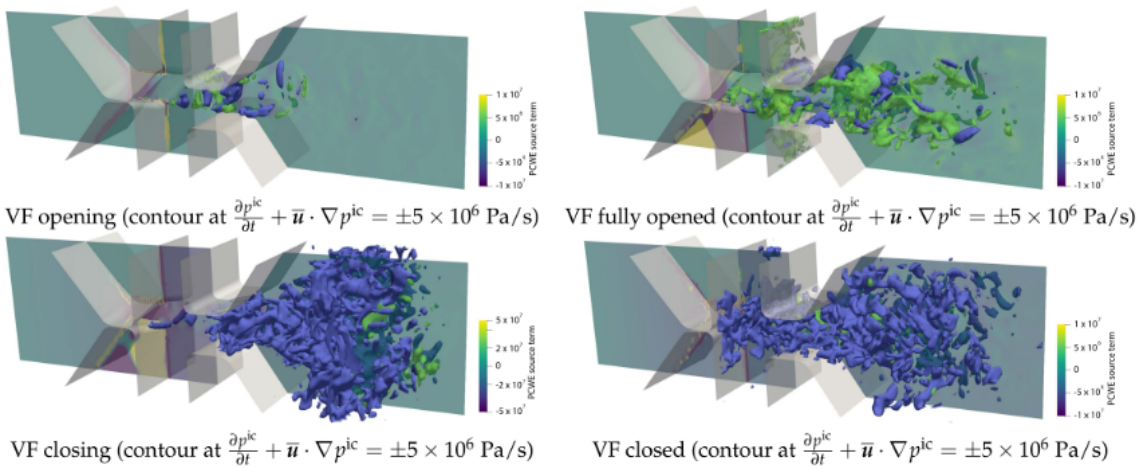


Figure 3.5: PCWE source terms during vocal fold oscillation. Extracted from [25].

Lasota *et al.* further contributed to the applicability of the PCWE for sound generation modeling by investigating the effect of the SGS (sub-grid scale) [73] and the anisotropic minimum dissipation [74] model.

In recent years, phonation modeling has increasingly combined numerical simulations with machine learning techniques to estimate biomechanical and aerodynamic parameters that govern voice production [55]. Early studies used probabilistic and optimization-based methods (e.g. in [75] and [76]), whereas more recent works have applied neural networks and reduced-order models. In these approaches, parameters such as subglottal pressure, glottal geometry, and tissue properties are estimated from simulated or experimental

data (e.g. [77, 78, 79]). Zhang developed a simulation-based machine learning framework [80, 81, 82] to estimate vocal fold physiology and subglottal pressure from acoustic output, addressing the inverse problem of voice production. Using a reduced-order model, a large dataset of 221,400 simulated vocal fold conditions was generated to train the neural network. Zhang's work demonstrate that data-driven and AI-assisted inverse modeling is emerging in the field of human phonation.

4 CAA model of human voice production

In this chapter, I present the implementation part of the proposed hybrid CAA framework for human voice production and the corresponding results I achieved. The workflow begins with a CFD investigation of how vocal fold vibrations influence the airflow through the larynx. The resulting flow field is then used as input for the acoustic simulations, which are carried out with the two configurations: stationary and moving acoustic grids. Although the modelling workflow is largely identical in both cases, the moving-grid formulation requires a more complex implementation, as it is not directly supported in openCFS. The resulting velocity and pressure fields, along with a comparison of the acoustic responses, are presented and discussed at the end of the chapter.

4.1 Methodology

For the CFD analysis, I used a simplified, 2D model of the laryngeal region, which was sufficient to compare different computational cases. The domain was built up and meshed using Coreform Cubit 2025.3, and the flow simulations were performed in the OpenFOAM v2412 environment. The mesh motion definition was realised by applying prescribed displacements to the boundaries representing the vocal folds. However, full closure could not be represented because this would result in excessive cell deformation or even collapse. Consequently, the glottal gap remained open with a time-varying cross-sectional area.

The acoustic wave propagation was modelled using the finite-element solver openCFS [8]. The incompressible pressure field obtained from the CFD simulation was used to compute acoustic source terms based on the PCWE, where the source terms were derived from the temporal evolution of the pressure field. Then, the dataset was transferred onto the acoustic mesh using CFS-Data [28], a pre- and postprocessing module of openCFS that enables consistent interpolation between the CFD and the acoustic domains. For the acoustic part, the computational domain was extended to include the vocal tract and the surrounding air region to capture relevant acoustic radiation effects.

In the moving-mesh acoustic configuration, the mesh motion was prescribed in a manner similar to that of the CFD model, using the SmoothPDE module of openCFS. The resulting time-dependent mesh was then decomposed into individual configurations for each time step using the pyCFS framework [83]. A dedicated Python workflow generated time-dependent XML input files for CFS-Data by linking each instantaneous pressure field to the corresponding acoustic mesh configuration. The processed data were assembled into a single transient dataset using PyCFS and were then used as input for the acoustic simulation. The AcousticPDE module of openCFS solved the acoustic problem. For the moving-grid case, SmoothPDE and AcousticPDE were coupled to ensure consistency between mesh deformation and acoustic wave propagation.

I investigated vocal fold oscillation frequencies of 100 Hz and 200 Hz, which represent the typical phonation ranges of males and females, respectively. CFD simulations were run for a total physical time of 0.3 seconds. To avoid initial transients, only the final 0.2 seconds of the pressure field were used to generate the source term and perform subsequent acoustic simulations. This ensured that the analysis was based on a fully developed periodic flow. Simulations were performed for both stationary and moving acoustic meshes at

each excitation frequency. The resulting acoustic fields were then compared to evaluate the impact of mesh motion on source interpolation and wave propagation. The results were post-processed and analyzed using ParaView and MATLAB.

4.2 Flow simulation

4.2.1 Boundary conditions

The domain boundaries shown in Figure 4.1 define the regions where the corresponding CFD boundary conditions are prescribed. These include the inlet and outlet boundaries, stationary walls, and the moving vocal fold surfaces (*VFu* for the upper and *VFl* for the lower folds), which modulate the glottal airflow periodically.

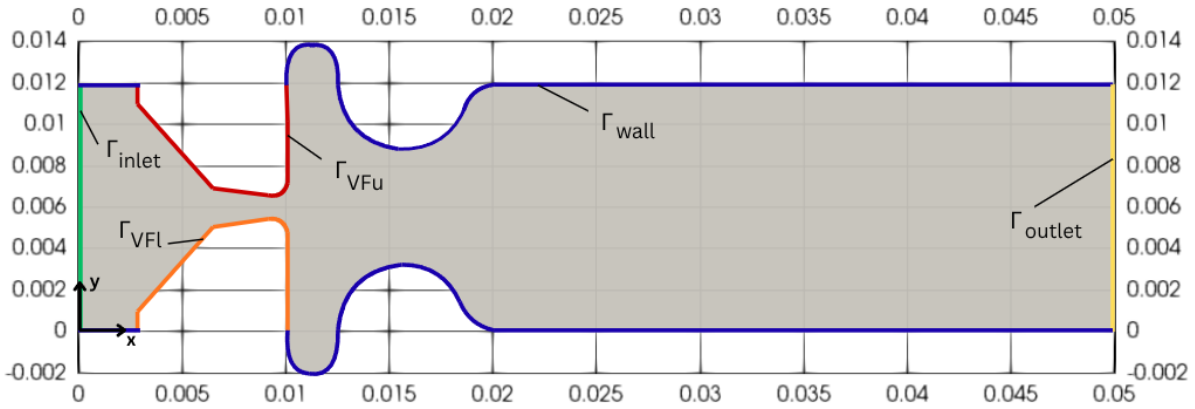


Figure 4.1: Boundary segments of the CFD domain. Grid dimension is given in [m].

Airflow is driven by a constant pressure difference between the inlet and outlet boundaries, which is a simplified approximation of physiological phonation conditions. Accordingly, a fixed pressure value of $p_{\text{inlet}} = 320$ Pa is prescribed at the inlet boundary Γ_{inlet}, while atmospheric reference pressure $p_{\text{outlet}} = 0$ Pa is applied at the outlet boundary Γ_{outlet}. The resulting pressure difference

$$\Delta p = p_{\text{inlet}} - p_{\text{outlet}} = 320 \text{ Pa} \tag{4.1}$$

drives the airflow through the glottal constriction, generating the pulsatile jet characteristic of phonation. Zero-gradient pressure conditions are prescribed on the stationary walls, denoted by Γ_{wall} as well as on the moving vocal fold surfaces, denoted by Γ_{VFu} and Γ_{VFl}.

For the velocity field, a zero-gradient condition is applied at the inlet,

$$\frac{\partial \mathbf{U}}{\partial n} = 0, \tag{4.2}$$

allowing the inflow velocity to develop naturally according to the instantaneous pres-

sure distribution and glottal opening. The stationary walls are modeled using a no-slip condition,

$$\mathbf{U} = 0. \tag{4.3}$$

The inletOutlet condition available in OpenFOAM is used at the outlet boundary. This boundary condition applies a zero-gradient formulation during outflow and a fixed, prescribed value during inflow. This ensures a physically consistent treatment of reverse flow at the boundary [84].

The oscillatory motion of the vocal folds is introduced by applying a prescribed mesh displacement field to the vocal fold boundaries, Γ_{VFu} and Γ_{VFl}. The displacement is implemented using a custom *codedFixedValue* boundary condition, based on the setup presented in [74] and implemented in consultation with the author.

The prescribed motion consists of a superposition of two harmonic oscillatory components defined around two characteristic points, $\mathbf{P}_1(6.4, 6, 0)$mm and $\mathbf{P}_2(9.2, 6, 0)$mm, as also shown in Figure 4.2.

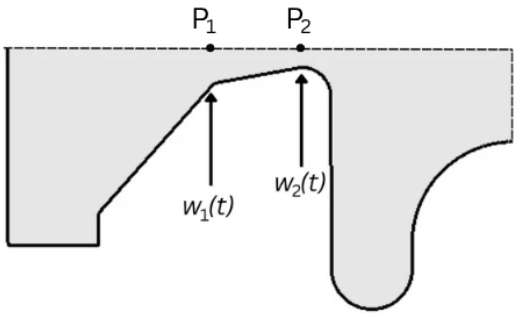


Figure 4.2: Characteristic points of prescribed vocal fold motion.

The vertical displacement is defined as a spatially weighted superposition of two harmonic contributions:

$$w(t, \mathbf{x}) = A_1 \alpha_1(\mathbf{x}) \sin(2\pi f t) + A_2 \alpha_2(\mathbf{x}) \sin(2\pi f t + \phi), \tag{4.4}$$

where A_1 and A_2 denote the displacement amplitudes, f is the oscillation frequency, and ϕ is the phase shift between the two contributions. The spatial weighting functions, α_1 and α_2, control the local distribution of the deformation and depend on the distance to the characteristic points, $\mathbf{P}_1$ and $\mathbf{P}_2$.

The phase shift is defined as

$$\phi = \frac{\pi}{2} \tag{4.5}$$

and the amplitudes are prescribed as $A_1 = 0.0002$ m and $A_2 = 0.0004$ m.

The spatial weighting functions are defined using exponential expressions as

$$\alpha_i(\mathbf{x}) = \exp\left(-\frac{\|\mathbf{x} - \mathbf{P}_i\|^2}{L^2}\right), \tag{4.6}$$

with a characteristic width of $L_\mathrm{c} = 2$ mm.

The motion is applied antisymmetricly with respect to the glottal midline. Therefore, the displacement of the upper and lower vocal fold boundaries is defined as

$$w_{\mathrm{VFu}}(t, \mathbf{x}) = w(t, \mathbf{x}), \tag{4.7}$$
$$w_{\mathrm{VFl}}(t, \mathbf{x}) = -w(t, \mathbf{x}), \tag{4.8}$$

resulting in opposite wall motions on the two sides of the glottis.

For illustrative purposes, the resulting vocal fold motion over one oscillation cycle is shown in Figure 4.3 at nine selected time instances.

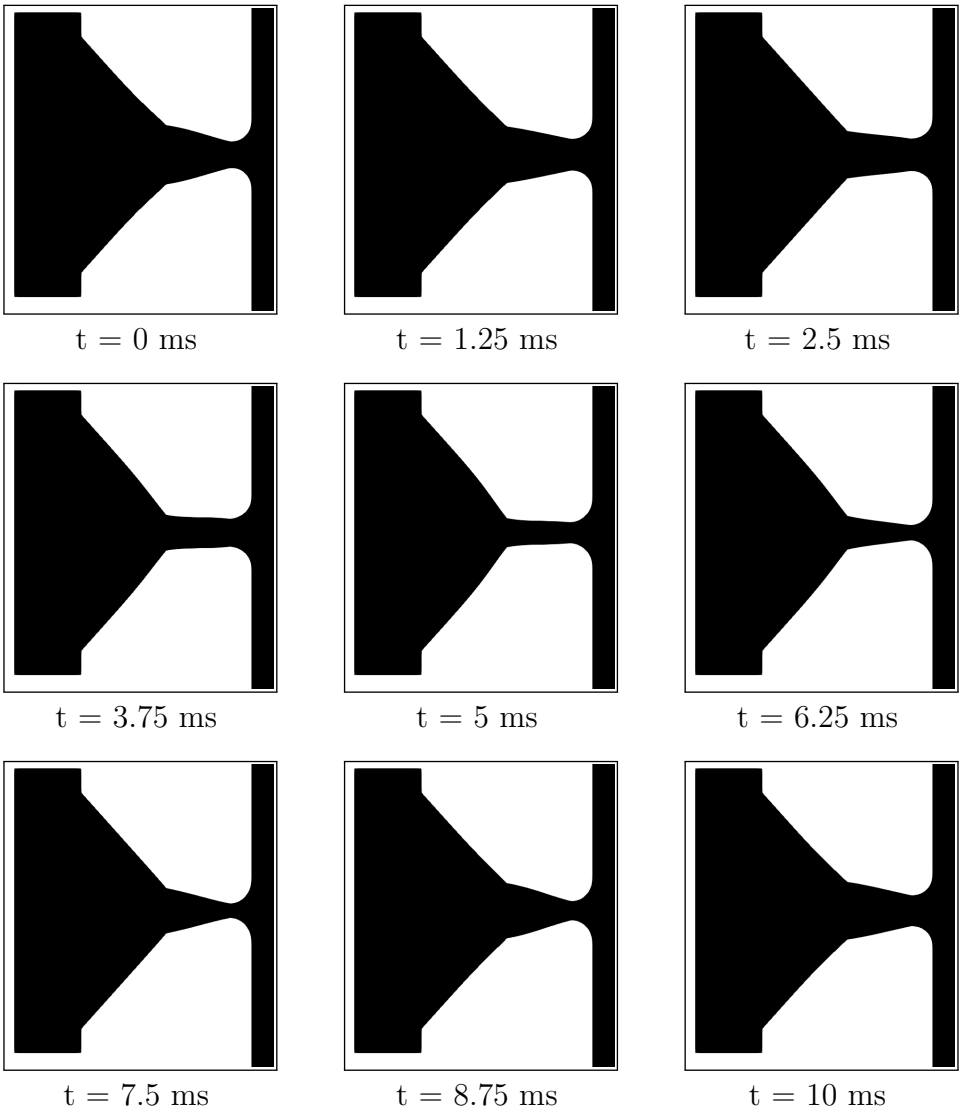


Figure 4.3: Characteristic motion phases of a vocal fold oscillation cycle.

4.2.2 Mesh definition

The computational mesh, illustrated in Figure 4.4, was generated using the automeshing tool of Cubit and consists of 32,348 quadrilateral elements across the entire domain. The domain is partitioned by vertical lines at $x = 6.4$ mm and $x = 15.65$ mm, a subregion with a higher mesh resolution that corresponds to the glottal area. In this region, the mesh resolution is increased locally to capture the steep expected gradients in the flow field. Boundary layer elements are applied along the vocal fold surfaces and stationary walls to improve near-wall resolution.

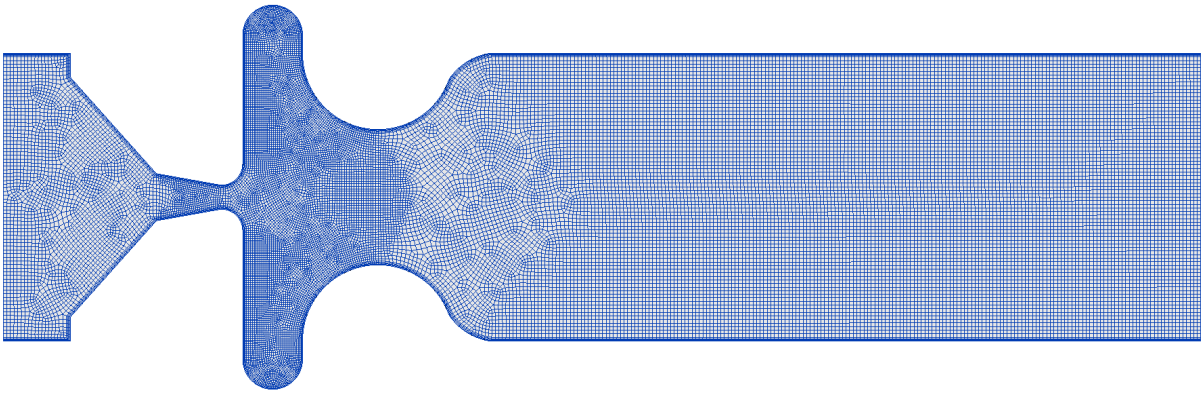


Figure 4.4: Meshed domain of the larynx geometry for CFD simulation.

Since simulation accuracy depends heavily on mesh quality, the relevant quality indicators for the initial configuration along with the boundary layer parameters are summarized in Table 4.1. Mesh distortion is typically evaluated using the skewness parameter, which offers a quantitative measure of element quality [85]. Excessively distorted elements may lead to nonphysical results, so their assessment is essential. For this reason, mesh skewness is evaluated at characteristic phases of the vocal oscillation cycle and visualized across the entire computational domain in Figure 4.5.

Table 4.1: CFD mesh quality indicators and boundary layer parameters.

Parameter	**Value**
Element type	Quad
Number of elements	32 348
Average skewness	3.37×10^{-2}
Maximum skewness	6.78×10^{-1}
Average aspect ratio	1.67
Maximum aspect ratio	5.04
First boundary layer thickness	0.3 mm
Boundary layer growth factor	1.2
Number of boundary layers	4

The skewness distribution of the CFD mesh is shown in Figure 4.5. To capture the effect of deformation over a full oscillation cycle, the initial configuration and the states corresponding to the maximum opening and closing of the glottis are included.

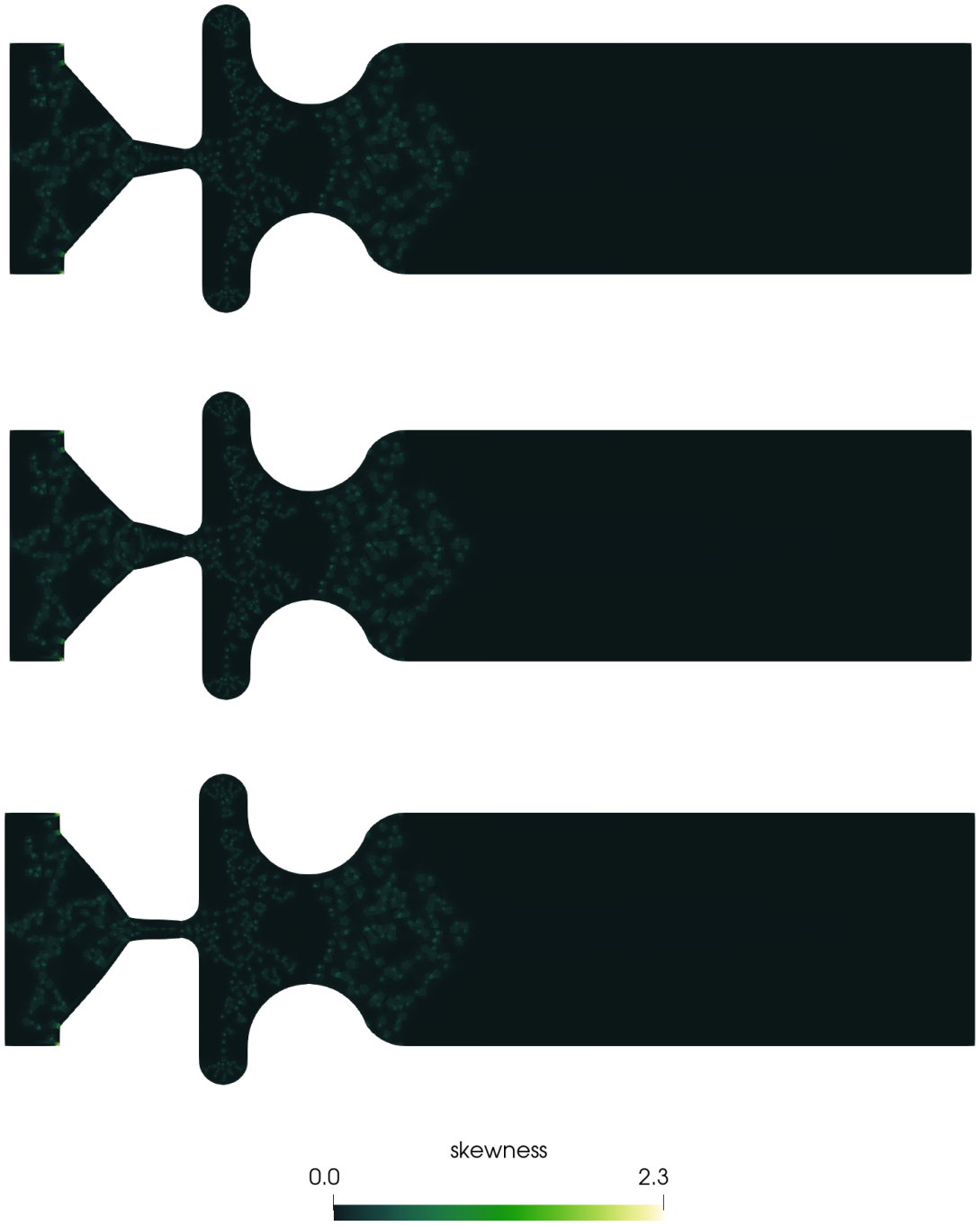


Figure 4.5: Skewness distribution of the CFD mesh at different phases of the glottal cycle: initial configuration (top), maximum opening (middle), and minimum opening (bottom).

The skewness values remain below 1 in most regions of the computational domain, indicating well-shaped elements and acceptable numerical quality. Only a small area in a sharp corner of the subglottal region exhibits higher distortion. However, this localized irregularity is not expected to significantly impact the acoustic results. Overall, the mesh quality is acceptable for CFD simulations.

4.2.3 Numerics and solver settings

The incompressible Navier–Stokes equations are solved using *pimpleFoam*, and mesh deformation is handled using the *displacementSBRStress* motion solver. Both of these are implemented in OpenFOAM. Air is modelled as a Newtonian fluid with a kinematic viscosity of

$$\nu = 10^{-5}\ \mathrm{m}^2/\mathrm{s}. \tag{4.9}$$

The flow is treated as laminar without turbulence modelling, as in many previous human phonation-related simulations using FVM (e.g.[69, 71, 86]). Adaptive time-step control is employed to maintain numerical stability. The time step size is automatically adjusted to satisfy the Courant–Friedrichs–Lewy (CFL) condition,

$$Co = \frac{u\Delta t}{\Delta x} < 1, \tag{4.10}$$

where u is the fluid velocity, Δt is the time step, and Δx is the characteristic mesh size. The initial time step is set to $\Delta t = 10^{-8}$ s, while the maximum allowed time step is $\Delta t = 10^{-5}$ s. Output data are written at intervals of 10^{-5} s for the subsequent acoustic analysis. A total physical simulation time of 0.3 s is computed, corresponding to 30 oscillation cycles in the case of a 100 Hz case and 60 cycles for the 200 Hz case.

4.3 Acoustic simulation on fixed grid

4.3.1 Computational domain

For the acoustic simulations, the laryngeal domain is extended to include the vocal tract and the surrounding air region in order to model acoustic wave propagation along the full sound path and to evaluate the radiated acoustic field in the ambient air.

The vocal tract geometry is based on the work of Story *et al.* [87], who derived simplified geometric representations of different vowels from MRI measurements. The vocal tract is divided into 46 equally spaced sections, each with a length of 0.396825 cm, with cross-sections defined by circular areas. In this study, the vowel /u/ is considered. Since a two-dimensional geometry is used, equivalent diameters are computed from the cross-sectional areas and used to construct the acoustic domain.

The cross-sectional area distribution for the vowel /u/ is shown in Table 4.2, while the full acoustic domain and its main computational regions are illustrated in Figure 4.6.

Table 4.2: Cross-sectional area distribution for the vowel /u/. Based on [87].

Sect.	Area [cm^2]	Sect.	Area [cm^2]	Sect.	Area [cm^2]	Sect.	Area [cm^2]
1	0.40	13	5.63	25	2.07	37	2.35
2	0.38	14	5.43	26	1.52	38	2.55
3	0.28	15	4.80	27	0.74	39	3.73
4	0.43	16	4.56	28	0.23	40	5.47
5	0.55	17	4.29	29	0.15	41	4.46
6	1.72	18	3.63	30	0.22	42	2.39
7	2.91	19	3.37	31	0.22	43	1.10
8	2.88	20	3.16	32	0.37	44	0.77
9	2.37	21	3.31	33	0.60	45	0.41
10	2.10	22	3.22	34	0.76	46	0.15
11	3.63	23	2.33	35	0.86		
12	5.86	24	2.07	36	1.82		

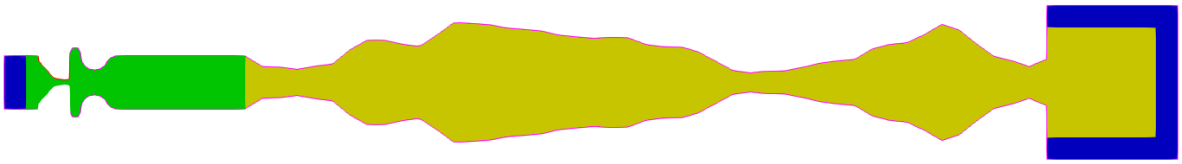


Figure 4.6: Acoustic domain and its main computational regions. Blue: Perfectly Matched Layer (PML) regions, green: laryngeal region, yellow: vocal tract and ambient air domain.

4.3.2 Boundary conditions and mesh

To suppress reflections at the two longitudinal ends (blue regions in Figure 4.6), Perfectly Matched Layer (PML) is applied. This boundary condition uses an inverse-distance-based damping formulation implemented in openCFS. The remaining boundaries, which are not explicitly specified, are treated as acoustically rigid (sound-hard) boundaries,

$$\nabla p_a \cdot n = 0, \tag{4.11}$$

corresponding to homogeneous Neumann conditions.

The acoustic mesh, consisting of 2,672 quadrilateral elements with a characteristic element size of 1.5 mm, is able to resolve wavelengths corresponding to frequencies of up to approximately 10 kHz, which is sufficient for human phonation simulations. The acoustic mesh is shown in Figure 4.7. In the glottal region, a locally refined mesh with a characteristic element size of 0.8 mm is used.

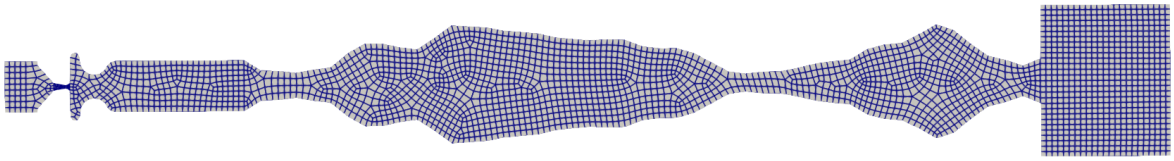


Figure 4.7: Meshed geometry of the computational acoustic domain.

4.3.3 Source term interpolation

Based on the PCWE formulation, the incompressible pressure field obtained from the CFD simulation is used to construct the acoustic source term. For the low Mach number regime considered in this work, convective contributions in the PCWE are neglected. The resulting source term reduces to the temporal derivative of the incompressible pressure field,

$$\dot{p}^{\mathrm{ic}} = \frac{\partial p^{\mathrm{ic}}}{\partial t}. \tag{4.12}$$

The scaling by fluid density and speed of sound, required for the final RHS formulation of the PCWE, is applied later during the acoustic simulation setup.

The time derivative is computed using a noise-robust differentiator implemented in openCFS. This reduces high-frequency numerical noise and preserves the signal low-frequency content of the signal. The differentiator is applied with order N = 5, resulting in the approximation

$$\dot{p}^{\mathrm{ic}} \approx \frac{2\left(p^{\mathrm{ic}}_{\mathrm{n+1}} - p^{\mathrm{ic}}_{\mathrm{n-1}}\right) + \left(p^{\mathrm{ic}}_{\mathrm{n+2}} - p^{\mathrm{ic}}_{\mathrm{n-2}}\right)}{8\Delta t}, \tag{4.13}$$

where Δt denotes the constant time step size and $n \pm k$ refers to time levels relative to the evaluation instant.

The resulting time derivative values computed on the CFD mesh are interpolated onto the acoustic mesh. Both meshes represent the same laryngeal geometry; however, the acoustic discretization uses a significantly coarser resolution. The difference in element size within the laryngeal region is illustrated in Figure 4.8.

The interpolation is performed in CFS-Data using the nearest neighbour technique. This approach was chosen because of its simplicity and robustness, even though it is less accurate than conservative interpolation schemes.

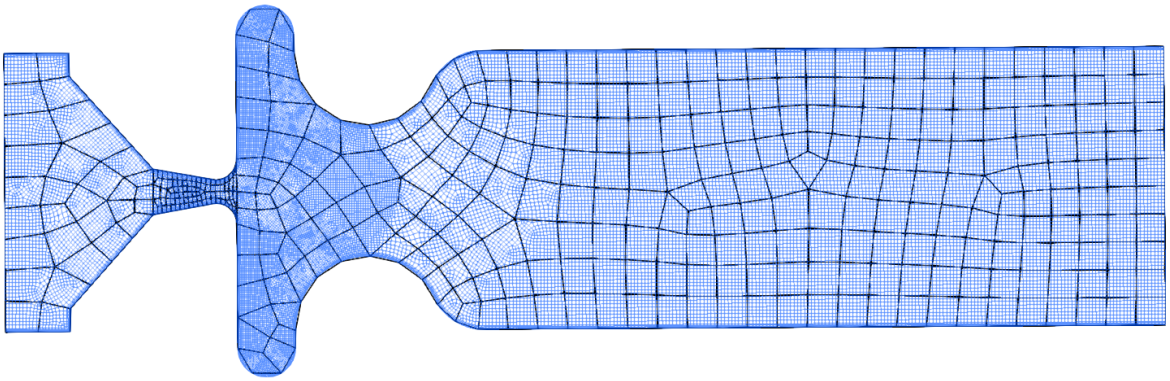


Figure 4.8: Comparison of spatial discretisation between CFD (blue) and acoustic (black) meshes in the laryngeal region.

4.3.4 Numerics and solver settings

The acoustic field was computed in openCFS using the acoustic potential formulation of the PCWE. The governing equation is given by

$$\left(\frac{1}{c_0^2}\frac{\partial^2}{\partial t^2} - \nabla^2\right)\psi_a = -\frac{1}{\rho_0 c_0^2}\frac{\partial p_{\mathrm{ic}}}{\partial t}, \tag{4.14}$$

where ψ_a denotes the acoustic potential. The acoustic pressure can be obtained as

$$p_a = \rho_0 \frac{\partial \psi_a}{\partial t}, \tag{4.15}$$

with ρ_0 being the density of air. The corresponding material properties are set to air at 20°C, with $\rho_0 = 1.204\ \frac{\mathrm{kg}}{\mathrm{m}^3}$ and $c_0 = 343.5\ \frac{\mathrm{m}}{\mathrm{s}}$.

The simulation is performed with a time step of

$$\Delta t = 10^{-5}\ \mathrm{s}, \tag{4.16}$$

using a total of 20,000 time steps, corresponding to the temporal resolution of the interpolated source data.

4.4 Acoustic simulation on moving grid

In the case of acoustic wave propagation computed on a moving mesh, the geometry, initial mesh, and boundary conditions are the same as in the earlier introduced fixed-mesh formulation. This section therefore presents the definition of mesh motion, as well as the computation of source terms and interpolation.

4.4.1 Mesh motion definition

The deformation of the acoustic mesh is prescribed using the SmoothPDE module of openCFS. The formulation is based on a quasi-static linear elasticity model in which inertial effects and external body forces are neglected. The governing equation is

$$\nabla \cdot \sigma = 0, \tag{4.17}$$

where σ denotes the Cauchy stress tensor. Assuming linear elastic material behaviour and small deformations, the mesh displacement is obtained from the prescribed boundary motion.

The vocal fold motion follows the same kinematic description as in the CFD model, including two spatially localized harmonic components acting at $\mathbf{P}_1$ and $\mathbf{P}_2$. The temporal evolution is defined by a combination of sine and cosine functions with a phase shift of

$$\phi = \frac{\pi}{2}, \tag{4.18}$$

between the two components. A total of 20,000 time steps are used, with a constant time increment of

$$\Delta t = 10^{-5}\ \text{s}, \tag{4.19}$$

ensuring consistency with the fluid mesh motion. The resulting mesh file contains a separate set of nodal coordinates for each time step, thereby defining a time-dependent displacement field.

4.4.2 Source term calculation and interpolation

The source term calculation and interpolation process using a moving acoustic grid requires three main steps after defining the mesh motion.

First, the mesh motion obtained from the SmoothPDE simulation is post-processed using the pyCFS framework. The nodal displacement field is read and the deformed node coordinates are reconstructed for each time step by adding the displacement field to the initial mesh coordinates. This procedure decomposes the transient moving mesh into a sequence of 20,000 static configurations, each of which represents the geometry of the oscillating vocal folds at a given time instant. The generated meshes are stored as individual *.cfs* files.

The aeroacoustic source terms are computed from the CFD pressure field using the CFS-Data pipeline, as in the fixed-grid case. For each CFD time step, the resulting

field is interpolated onto the corresponding deformed acoustic mesh using the nearest neighbour interpolation scheme. This process is automated using a Python script, which generates the required XML input file for each time step and assigns the corresponding target mesh and CFD time window to evaluate the temporal derivative. A sliding window of ± 10 time steps is used to provide the necessary temporal neighborhood for the finite-difference scheme. The results are stored as interpolated individual source fields.

Finally, the interpolated result files are merged into a single transient dataset using pyCFS. This dataset contains the time-dependent aeroacoustic source field mapped onto the moving acoustic mesh and can be used as input for the subsequent acoustic wave propagation simulation.

Figure 4.9 shows an overview of the complete workflow of the moving-grid case, from acoustic mesh movement definition to acoustic wave propagation simulation.

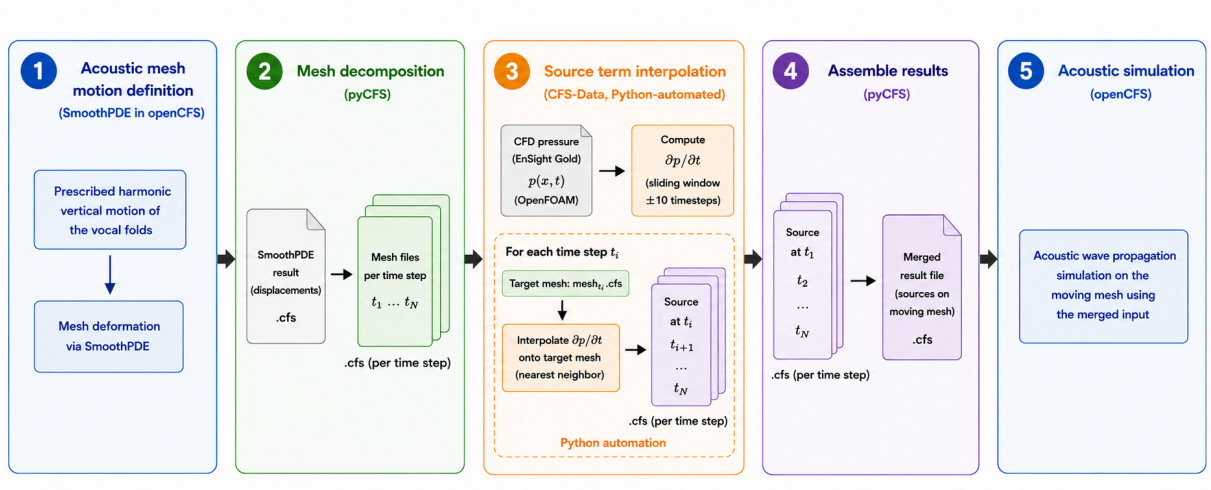


Figure 4.9: Workflow of the acoustic simulation using a moving grid.

4.4.3 Solver settings and methods

The acoustic setup for the moving-grid simulations remains identical to that for the fixed-grid case. The main difference is the use of a time-dependent computational mesh, which allows the acoustic domain to follow the prescribed vocal fold motion.

The interaction between the motion of the mesh and acoustic propagation is realized through one-way coupling of their descriptive equations. For each time step, the mechanical equation (4.17) is solved first, followed by the PCWE on the updated mesh configuration. After each time step, the geometry of all regions is updated according to the computed mesh deformation.

Similarly to the fixed grid case, a total of 20,000 time steps are simulated with intervals of

$$\Delta t = 10^{-5} \text{ s}. \tag{4.20}$$

4.5 Results

The results of the CAA simulations are presented below. The velocity and pressure fields for the two cases of vocal fold excitation frequency are introduced from the CFD results. The resulting acoustic potential, calculated on fixed and moving acoustic grids, is shown for 100 Hz. Then, a direct comparison of the fixed and moving acoustic grid formulations is performed based on the resulting acoustic pressure signals and their spectral analysis.

It should be noted that the velocity and pressure fields, as well as the acoustic potential distributions presented in the following, correspond to single representative oscillation cycles. These results are intended to illustrate characteristic instantaneous flow and acoustic structures, but should not be interpreted as globally valid values over the entire simulation. The representative cycles shown for different excitation frequencies correspond to the same physical time instant within the simulation and therefore represent different oscillation cycle numbers. For the quantitative comparison of the fixed and moving acoustic grid formulations, the acoustic pressure signals and their frequency spectra are evaluated using the full simulation time.

4.5.1 Velocity fields

For the visualization of the velocity field, the oscillation starting at $t = 0.1$ s was selected. This allows sufficient time for the flow field to fully develop and reach a representative state. Additionally, numerical artifacts associated with the initial phase no longer significantly affect the results.

The CFD results show that the periodic motion of the vocal folds generates a strongly unsteady flow through the glottal constriction. The flow can be characterized by the periodic opening and closing of the glottis as a pulsatile jet in the supraglottal region. Vortical structures emerge, which serve as the main source of the resulting sound.

For the 100 Hz excitation case, the velocity field is displayed in Figure 4.10 at four uniformly distributed time instants. A high-speed jet develops in the glottal channel with a peak velocity of approximately 48 m/s, which falls into a realistic range, proving the incompressible flow assumption

$$Ma = \frac{U_{\max}}{c_0} < 0.3 \tag{4.21}$$

to be valid. Downstream of the glottis, recirculation zones appear near the false vocal folds.

At 200 Hz, the overall flow topology, displayed in Figure 4.11, remains similar. However, vortex dynamics is more compact and temporally concentrated, and a larger coherent vortical structure can be observed in the central region of the supraglottis. A second vortex can be seen further downstream of the vocal folds, which can be attributed to the vortex shed during the preceding oscillation cycle. The higher excitation frequency results in more rapidly evolving flow structures.

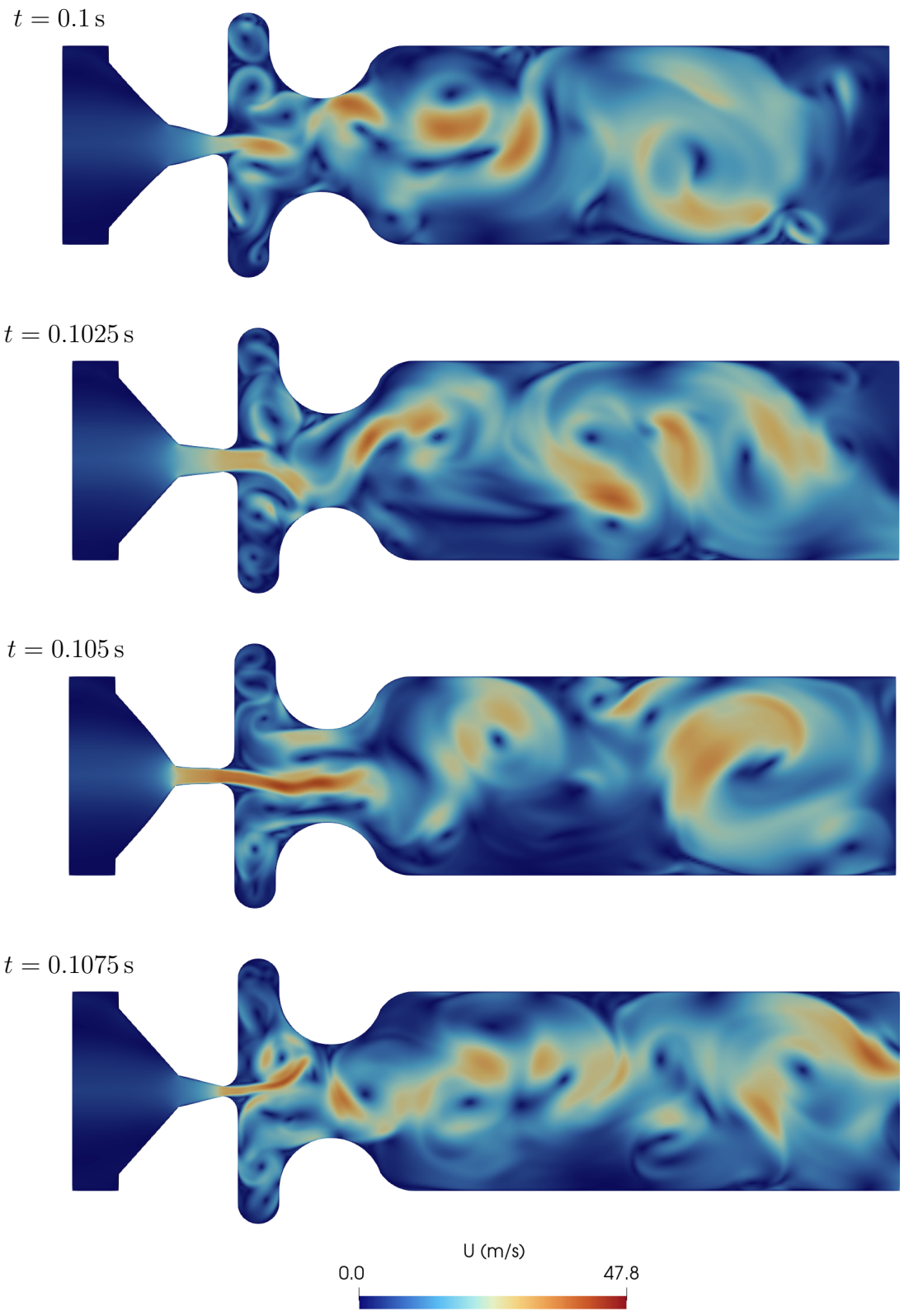


Figure 4.10: Velocity fields at characteristic time instants corresponding to the fully opened state, closing phase, near-closure state, and opening phase of the glottal gap (from top to bottom, respectively) for 100 Hz excitation case.

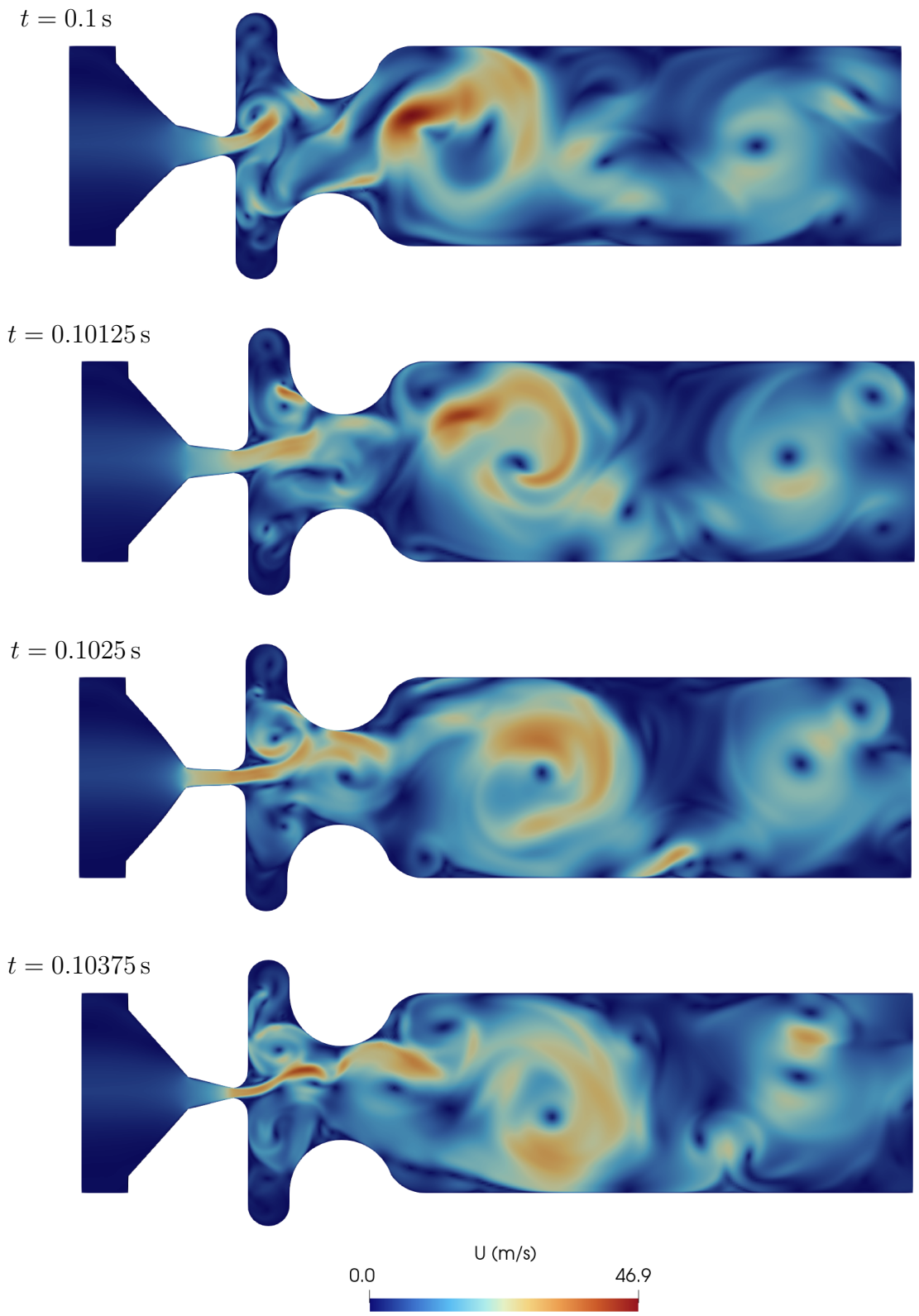


Figure 4.11: Velocity fields at characteristic time instants corresponding to the fully opened state, closing phase, near-closure state, and opening phase of the glottal gap (from top to bottom, respectively) for 200 Hz excitation case.

4.5.2 Pressure field

The pressure field is plotted the oscillation starting at $t = 0.1$ s and evaluated at the same time instants as the velocity fields. The pressure distributions for the 100 Hz and 200 Hz cases are shown in Figure 4.12 and Figure 4.13, respectively.

The pressure distribution throughout the laryngeal model is primarily governed by the imposed pressure difference of 320 Pa between the inlet and outlet. The 100 Hz case exhibits a pressure range of approximately -900 Pa to 330 Pa, while the 200 Hz case has a wider range of approximately -1200 Pa to 330 Pa. Upstream of the glottis, the pressure field remains nearly uniform, which indicates a stable enforcement of the prescribed boundary conditions. Downstream of the glottal constriction, the pressure gradually recovers toward ambient conditions. In both cases, regions of strongly negative pressure are spatially localized and coincide mainly with the vortex cores. Furthermore, the pressure field downstream of the glottis fluctuates around an ambient level.

The showcased CFD results of velocity and pressure confirm that the flow features are physiologically realistic and consistent with known phonation mechanisms.

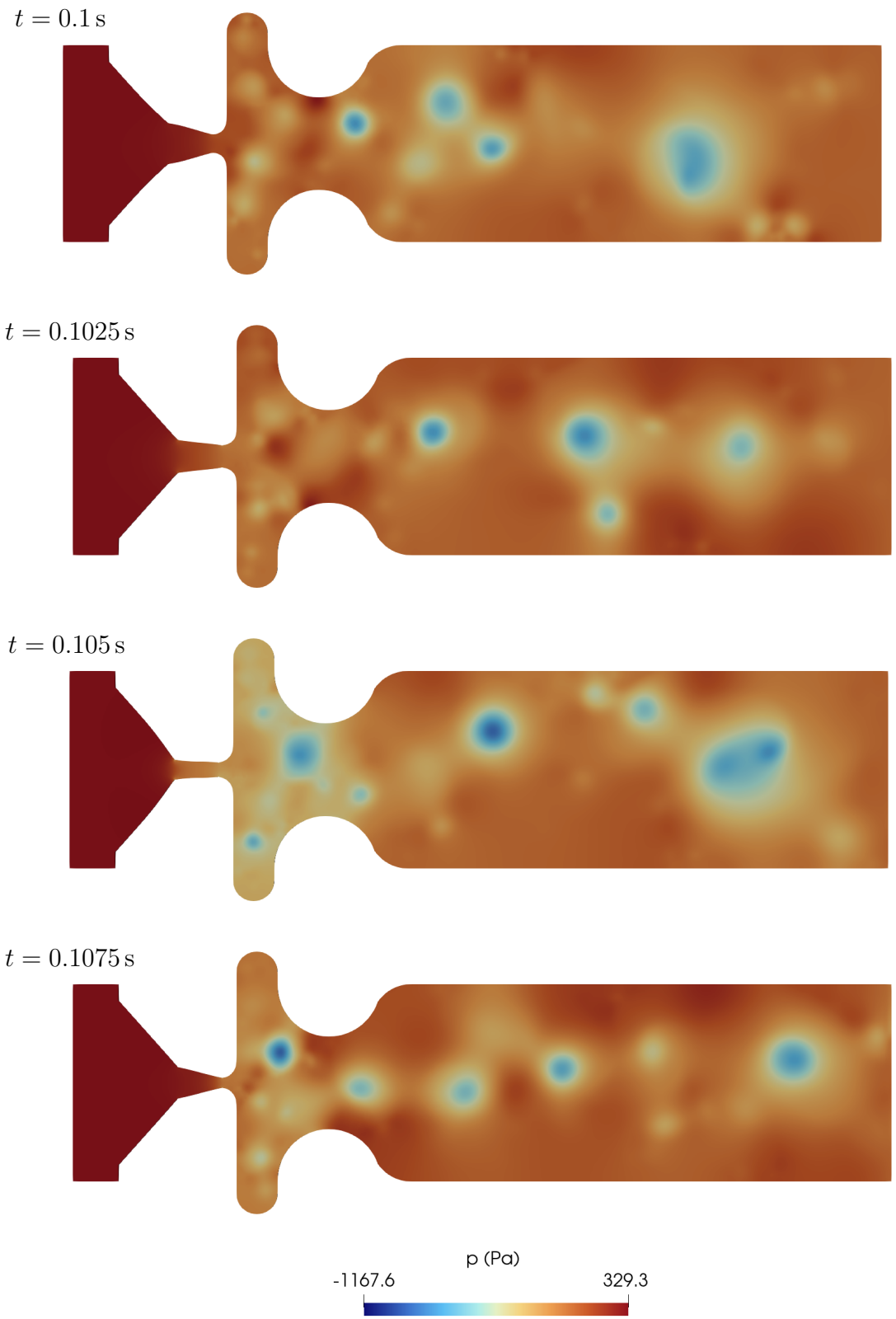


Figure 4.12: Pressure fields at characteristic time instants corresponding to the fully opened state, closing phase, near-closure state, and opening phase of the glottal gap (from top to bottom, respectively) for 100 Hz excitation case.

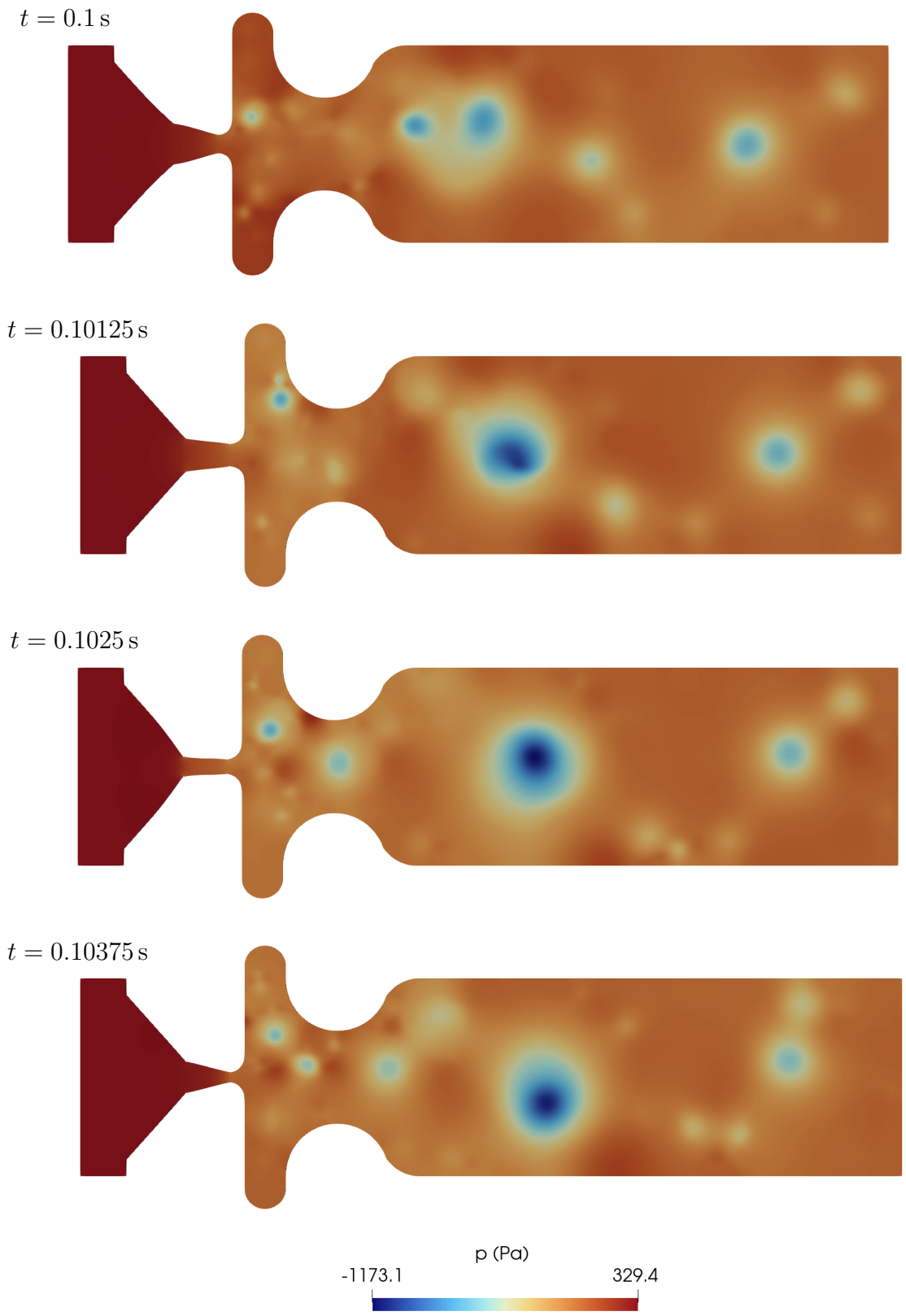


Figure 4.13: Pressure fields at characteristic time instants corresponding to the fully opened state, closing phase, near-closure state, and opening phase of the glottal gap (from top to bottom, respectively) for 200 Hz excitation case.

4.5.3 Wave propagation

The acoustic field is characterized by the acoustic potential, which is the primary unknown of the applied PCWE formulation. One oscillation cycle is evaluated at eight uniformly distributed time instants, starting at $t = 0.2$ s. The colour scales are adjusted for the individual time instants in order to improve the visualization of the propagating wave structures.

The propagating acoustic wave structure for the 100 Hz excitation case is shown in Figure 4.14 and Figure 4.15, corresponding to simulations performed on fixed and moving grids, respectively. The results exhibit clear wave-like propagation through the vocal tract domain, with the acoustic potential varying approximately between -9×10^{-6} m^2/s and 10^{-4} m^2/s. Both cases are characterized by smooth transitions between regions of positive and negative ψ_a values. The results suggest a characteristic wavelength of about 13 cm, consistent with the local peak observed around 2500 Hz in the subsequent fast Fourier transform (FFT) analysis. This confirms the consistency between the time-domain and frequency-domain representations of the acoustic field.

Comparing fixed and moving acoustic grids shows that the overall wave structure remains largely unchanged. The moving mesh introduces only minor phase shifts and local amplitude; however, it does not affect the global propagation characteristics.

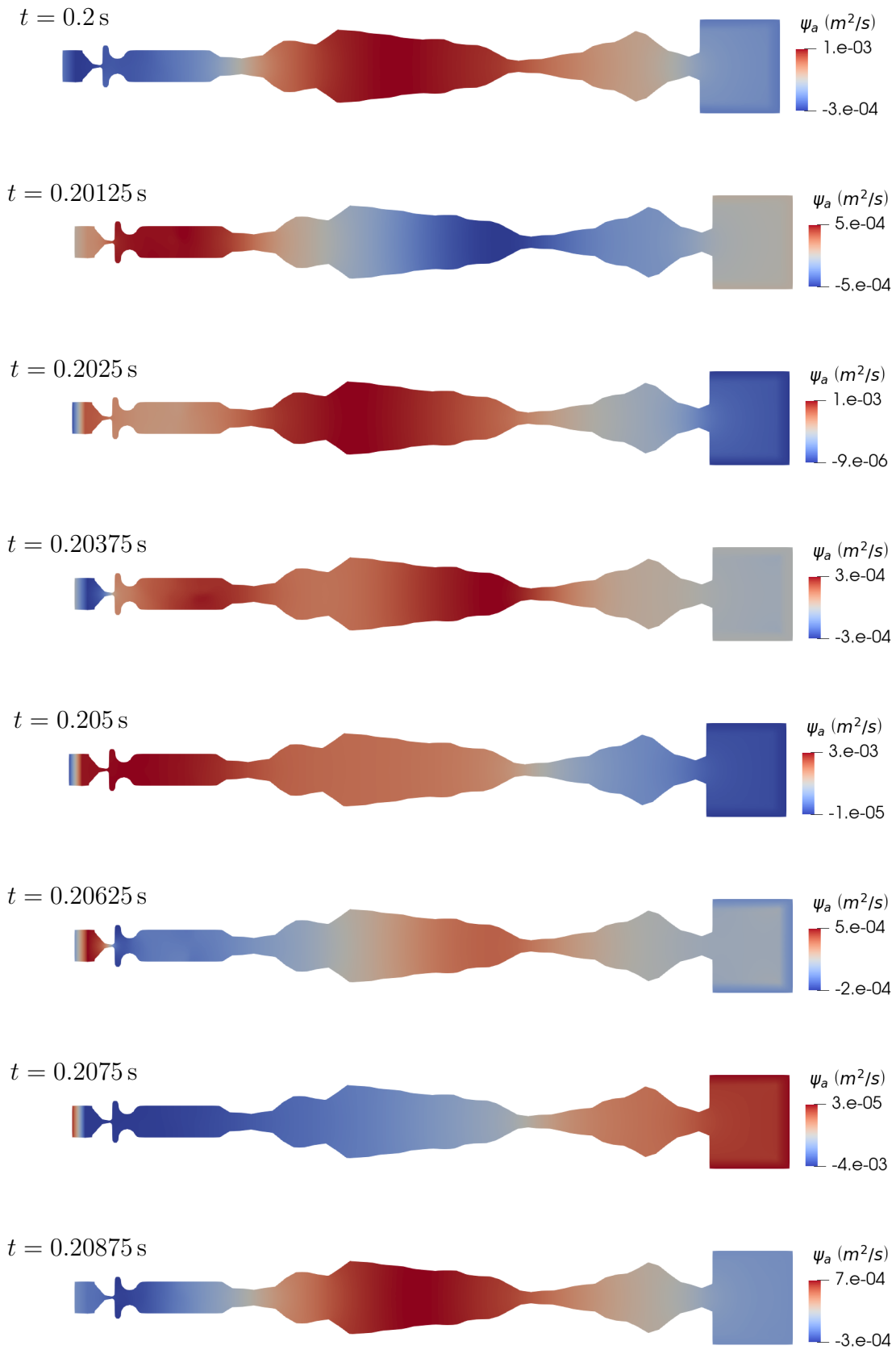


Figure 4.14: Acoustic potential fields at eight representative time instants over one oscillation cycle for the 100 Hz excitation case, calculated on fixed grid.

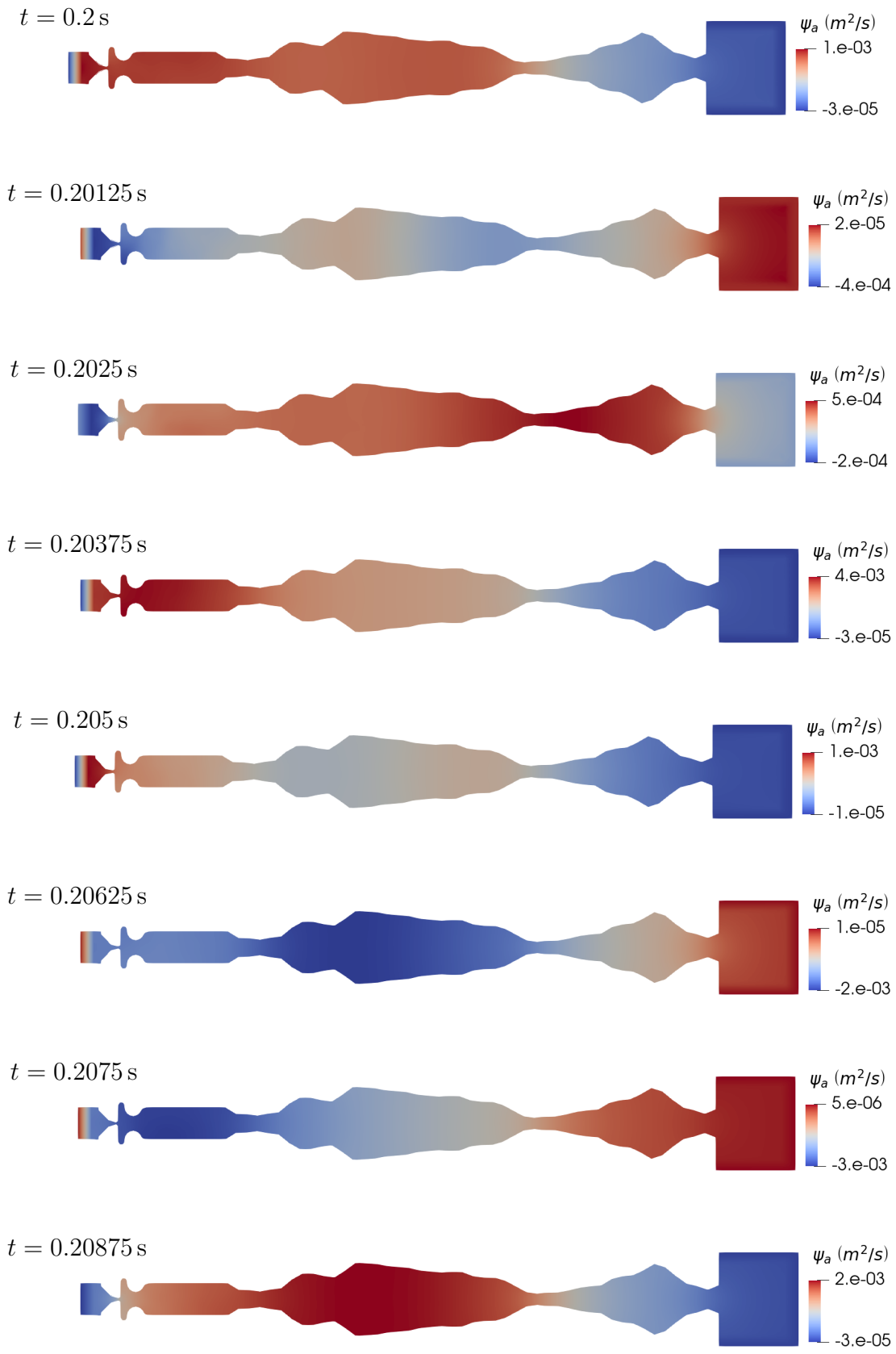


Figure 4.15: Acoustic potential fields at eight representative time instants over one oscillation cycle for the 100 Hz excitation case, calculated on moving grid.

4.5.4 Acoustic pressure

Acoustic pressure is evaluated in the surrounding air domain at a monitoring location positioned 1 cm downstream of the vocal tract outlet. Results for the 100 Hz and 200 Hz excitation cases are shown in Figure 4.16 and Figure 4.17, respectively. The acoustic pressure signals obtained from the simulations have low amplitudes, typically ranging between -2 Pa and $+2$ Pa. Peaks of up to approximately ± 4 Pa are occasionally observed; however, they are sporadic and do not occur consistently across oscillation cycles. Direct comparison of the fixed-grid and moving-grid formulations shows that both approaches yield nearly identical acoustic pressure amplitudes; however the signals are not aligned in time.

The results presented here cover the full acoustic simulation window, which corresponds to the final 0.2 s of the CFD simulation.

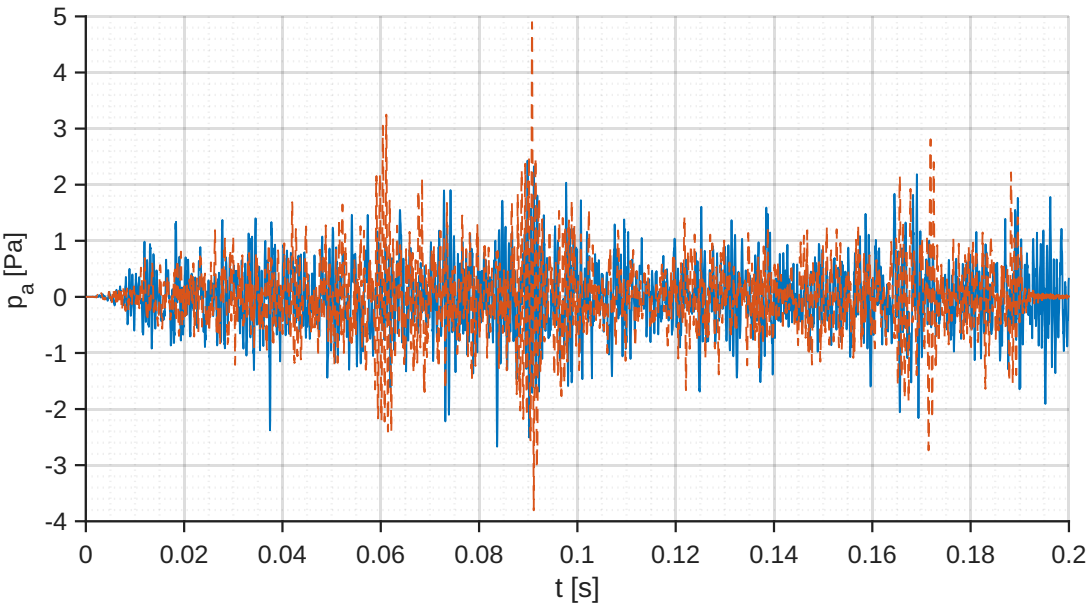


Figure 4.16: Acoustic pressure signals for fixed (blue) and moving (orange) grids, measured at a monitoring point located 1 cm downstream of the vocal tract outlet (100 Hz excitation case).

It can be observed that the acoustic pressure magnitudes are several orders of magnitude smaller than the characteristic pressure levels of the main flow field. This significant scale separation is consistent with the assumptions of the applied perturbation ansatz, providing additional confirmation of the physical and numerical correctness.

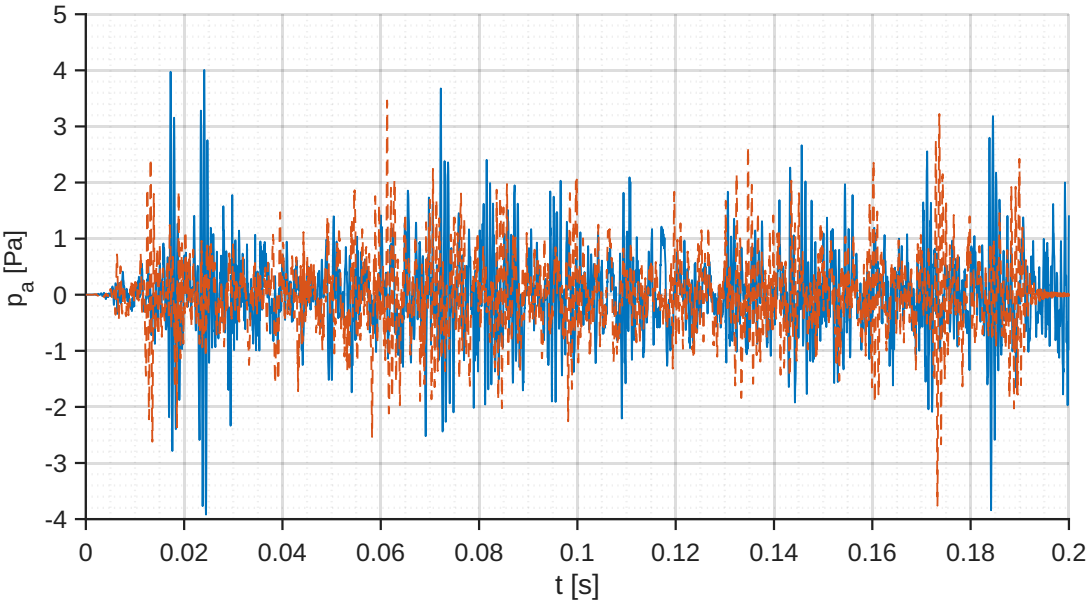


Figure 4.17: Acoustic pressure signals for fixed (blue) and moving (orange) grids, measured at a monitoring point located 1 cm downstream of the vocal tract outlet (200 Hz excitation case).

4.5.5 Frequency spectra

The acoustic pressure computed and visualized in the time domain can also be represented in the frequency domain with the help of FFT. The dominant frequency contributions can be thus identified in the acoustic field through the decomposition of the transient signal into a sum of trigonometric functions.

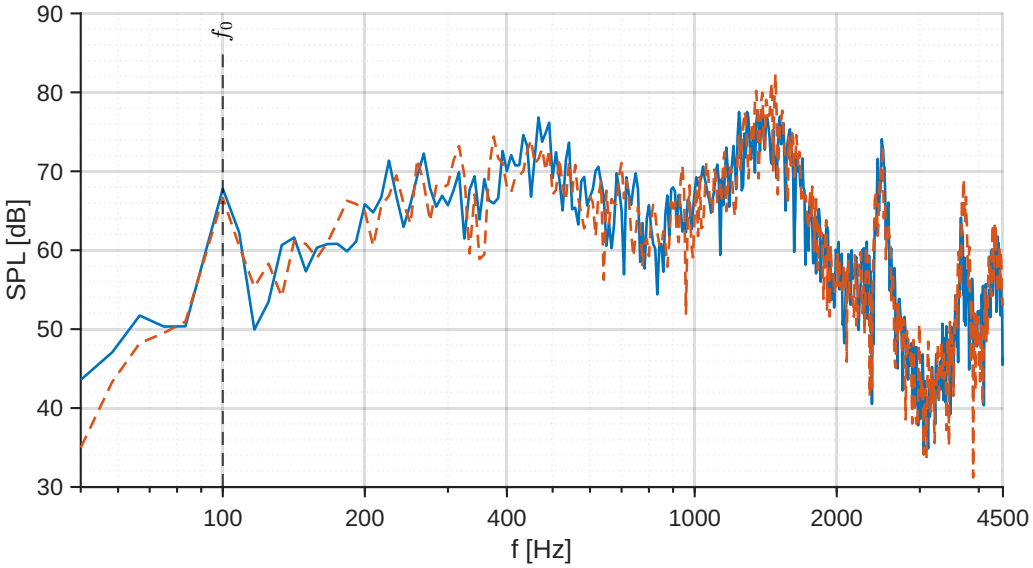


Figure 4.18: Frequency spectrum for fixed (blue) and moving (orange) grids, measured at a monitoring point located 1 cm downstream of the vocal tract outlet (100 Hz excitation case) The fundamental frequency is marked by f_0.

.

The spectrum results are presented in Figure 4.18 for the 100 Hz case and in Figure 4.19 for the 200 Hz case. The sound pressure level values are being calculated based on (2.28), using a reference pressure of $p_{ref} = 20$ μPa.

The frequency spectra of the acoustic pressure signals clearly reveal the fundamental frequencies of 100 and 200 Hz, which correspond to the prescribed vocal fold excitation frequencies. Several higher-frequency peaks are also evident in both excitation cases, most notably at 1450 Hz, 2500 Hz, and 3700 Hz.

The observed peaks are consistent with vocal tract filtering effects, meaning that the vocal tract geometry selectively amplifies specific frequency bands, while filters out others. Since the spectral peak with highest amplitude turned to be at 1450 Hz, it is primarily attributed to the filtering effect of the vocal tract. Similarly, the peaks around 2,500 Hz and 3,700 Hz are indicative of higher-order resonant modes. Thus, it is clearly demonstrated that the radiated sound is governed by both the excitation source and the frequency-dependent transfer characteristics of the vocal tract.

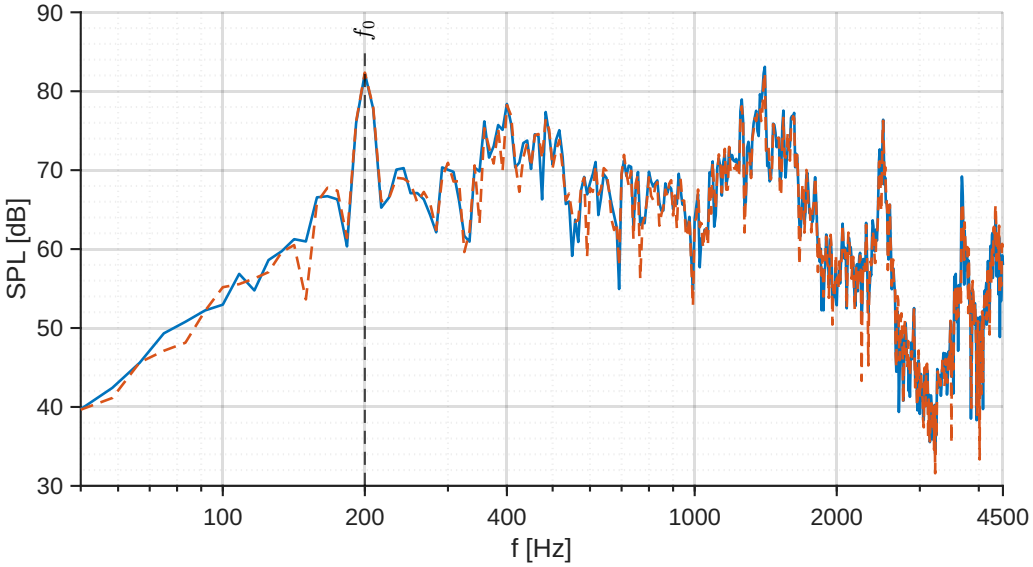


Figure 4.19: Frequency spectrum for fixed (blue) and moving (orange) grids, measured at a monitoring point located 1 cm downstream of the vocal tract outlet (200 Hz excitation case). The fundamental frequency is marked by f_0.

.

Comparison of the fixed and moving acoustic mesh formulations reveals only minor differences across the entire frequency spectrum. Deviations at the dominant resonance peaks are negligible. Consequently, for the investigated configuration and excitation frequencies, the use of a moving acoustic mesh does not provide any advantage over the fixed-grid formulation in terms of the predicted acoustic pressure spectrum.

5 Summary

5.1 Results

The primary objective of the thesis was to develop and implement a hybrid computational aeroacoustic framework, capable of handling moving acoustic meshes. For a simulation of human voice production, the influence of acoustic mesh motion was compared to the case where fixed acoustic mesh is used throughout. To achieve this, a partitioned numerical workflow was established by coupling incompressible CFD simulations with acoustic wave propagation simulations, carried out in openCFS using the Perturbed Convective Wave Equation. In addition to the conventional approach employing a fixed acoustic mesh, a novel workflow was developed that allows for source term interpolation and acoustic wave propagation on deforming acoustic meshes.

The CFD simulations reproduced the characteristic flow phenomena associated with phonation. The periodic motion of the vocal folds generated a pulsatile jet through the glottal constriction and led to the formation of vortical structures in the supraglottal region. These flow structures represent the primary mechanism responsible for aerodynamic sound generation. The obtained velocity fields exhibited peak values of approximately 45 m/s, remaining within the low Mach number regime and therefore confirming the validity of the incompressible flow assumption. The pressure fields showed realistic distributions, with localized regions of negative pressure associated with vortex cores. Overall, the CFD results demonstrated physically plausible behaviour and were consistent with established descriptions of the phonatory flow.

The acoustic simulations confirmed that the pressure fluctuations generated by the flow field act as effective sound sources within the PCWE framework. The propagation of acoustic waves through the vocal tract and into the surrounding air domain was successfully captured for both investigated excitation frequencies. The computed acoustic pressure amplitudes were significantly smaller than the characteristic hydrodynamic pressure levels of the flow field, supporting the assumptions of hybrid CAA and demonstrating its consistency.

The frequency-domain analysis revealed that the acoustic components corresponding to the prescribed vocal fold oscillation frequencies of 100 Hz and 200 Hz are dominant. In addition to these fundamental frequencies, several higher-frequency peaks were identified, around 1450 Hz, 2500 Hz, and 3700 Hz. These peaks are attributed to frequency-selective filtering within the vocal tract.

The developed workflow successfully enabled the interpolation of source terms onto time dependent acoustic meshes and the subsequent simulation of acoustic wave propagation on deforming domains. Comparison of the results obtained with fixed and moving acoustic meshes showed that the overall acoustic behaviour remained largely unchanged. The acoustic potential distributions exhibited similar propagation patterns, while the acoustic pressure signals and their corresponding frequency spectra showed only minor differences. Deviations in the dominant spectral peaks were negligible, and no significant changes in acoustic amplitudes were observed. For the investigated configuration, the influence of acoustic mesh motion on the predicted acoustic field remained limited, which may be primarily attributed to the compact nature of the acoustic sources.

5.2 Conclusion and outlook

The results show that the framework captures the main physical mechanisms of phonation, such as pulsatile jet formation, vortex generation, and sound propagation through the vocal tract. The simulations reproduced both the prescribed excitation frequencies and the main resonance frequencies of the vocal tract, demonstrating that the hybrid approach can represent the essential aeroacoustic behavior of voice production.

The comparison between fixed and moving acoustic meshes showed that acoustic mesh motion had only a minor influence on the predicted acoustic field for the investigated cases. The resulting acoustic pressure signals, wave propagation patterns, and frequency spectra were nearly identical. Consequently, no clear advantage of the moving acoustic mesh formulation could be identified for the simplified two-dimensional model and excitation frequencies considered in this study. Nevertheless, the developed methodology extends the existing computational framework by enabling simulations of deforming acoustic domains that were previously not possible within the adopted workflow.

Several limitations of the present work should be acknowledged. The simulations were performed on a simplified two-dimensional geometry and employed prescribed vocal fold motion rather than a fully coupled fluid–structure interaction model. Furthermore, complete closure of the glottal gap could not be represented because of mesh quality constraints. These simplifications were necessary to maintain computational feasibility and to focus on the methodological development of the moving-mesh aeroacoustic framework.

Future work may therefore proceed in several directions. A natural extension would be the application of the developed workflow to anatomically realistic three-dimensional geometries, where the influence of acoustic mesh motion may become more pronounced. Incorporating fully coupled fluid–structure interaction models would enable more realistic representations of vocal fold dynamics and potentially improve the prediction of sound generation mechanisms. Further investigations could also examine larger deformation amplitudes and more realistic geometries reconstructed from medical imaging data. In addition, the developed methodology may be applied to other aeroacoustic problems involving moving boundaries, extending its usefulness beyond the field of phonation modelling.

In conclusion, this thesis contributes to the numerical modelling of human voice production through the development and validation of a hybrid aeroacoustic framework capable of handling moving acoustic meshes. The proposed framework provides a basis for future investigations of more realistic phonation scenarios.

Összefoglaló

Az emberi hangképzés az aeroakusztika, vagyis az áramlástan és akusztika kapcsolatával foglalkozó tudományterület egyik jellegzetes példája. A gégében elhelyezkedő hangszálak rezgése az addig közel egyenletesen áramló levegőt örvényes, turbulens áramlássá alakítja. Ennek hatására jelentős nyomásingadozások lépnek fel, amelyek aeroakusztikai forrásként működve hanghullámokat keltenek. A keletkező hullámok a száj- és orrüreg csatornáin áthaladva módosulnak, így alakul ki a végső beszédhang. A jelenség élő szervezetben történő kísérleti vizsgálata a nehéz hozzáférhetőség miatt jelentős korlátokba ütközik, ezért a fizikai mechanizmusok részletes feltárása máig nem tekinthető teljesnek. Az utóbbi évtizedekben a numerikus modellezési módszerek fejlődése ugyanakkor új lehetőségeket teremtett a hangképzés mérnöki szemléletű vizsgálatára és mélyebb megértésére.

Napjainkban a legelterjedtebb megközelítés az ún. hibrid aeroakusztikai módszer, amely az áramlási és akusztikai mezők elkülönített kezelésén alapul. A számítás első lépéseként az áramlási mező kerül meghatározásra numerikus szimuláció vagy kísérleti mérés segítségével. Ezt követi az akusztikai tér számítása, amely az eltérő tér- és időskálák miatt általában külön hálón történik. Mivel a hangterjedés numerikus leírása rendszerint kisebb felbontást igényel, ehhez egy ritkább háló is elegendő, ami egy közbenső lépésként szükségessé teszi az áramlástani eredmények átvitelét az akusztikai hálóra. A szakirodalomban bemutatott hibrid aeroakusztikai alkalmazások esetében mind az interpoláció, mind az akusztikai számítás rögzített akusztikai hálón történik. A hangképzés során azonban a hangszalagok mozgásának következtében a geometria folyamatosan változik, ami befolyásolhatja a hanghullámok terjedését. Ez alapján feltételezhető, hogy a jelenség pontosabb leírása érhető el, ha az akusztikai számítás időben változó, mozgó hálón történik. Diplomadolgozatom célja egy olyan hibrid aeroakusztikai számítási eljárás fejlesztése és implementálása volt, amely a hangképzés modellezése során képes figyelembe venni az időben változó geometria hatását. A folyamat során az áramlási tér meghatározása összenyomhatatlan közeget feltételező CFD szimulációval történt, míg a hangterjedés leírására a PCWE (Perturbed Convective Wave Equation) aeroakusztikai formuláció szolgált. A dolgozat központi eleme egy olyan automatizált számítási folyamat fejlesztése volt, mely lehetővé teszi az akusztikai forrástagok időben változó hálóra történő átvitelét, valamint a hangterjedés szimulációját ezen a hálón. A fejlesztett módszerrel rögzített és mozgó akusztikai hálón végzett szimulációk eredményeit hasonlítottam össze a hálómozgás akusztikai térre gyakorolt hatásának értékelése céljából.

A CFD számítások reprodukálták a hangképzés során kialakuló jellegzetes áramlási jelenségeket, míg az akusztikai szimulációk sikeresen leírták a hanghullámok terjedését. A frekvenciaanalízis során a hangszálrezgés alapfrekvenciái mellett a hangcsatorna szűrőhatásából eredő magasabb frekvenciájú összetevők is azonosíthatóak voltak. A rögzített és mozgó akusztikai hálóval kapott eredmények összehasonlítása alapján a hálómozgás hatása a vizsgált esetekben elhanyagolhatónak bizonyult, ami elsősorban az akusztikai források kompakt jellegével magyarázható. A dolgozat eredményeként megvalósult egy általános hibrid aeroakusztikai keretrendszer, amely lehetővé teszi mozgó hálók vizsgálatát és alapot teremt összetettebb, a valósághoz közelebb álló hangképzési modellek jövőbeli elemzéséhez.

Kulcsszavak: aeroakusztika, hangképzés, interpoláció, openCFS

References

[1] https://stateopera.com.au/graham-abbott-on-richard-strauss. Accessed: 2026-04-10.

[2] Viveka Lyberg Åhlander, Roland Rydell, Peeter Fredlund, and Staffan Wilén. Prevalence of voice disorders in the general population, based on the stockholm public health cohort, 08 2019.

[3] Stefan Kniesburges, Scott L. Thomson, Anna Barney, Michael Triep, Petr Sidlof, Jaromir Horacek, Christoph Brucker, and Stefan Becker. In vitro experimental investigation of voice production. *Current Bioinformatics*, 6(3):305–322, 2011.

[4] Jan Valášek and Petr Sváček. Numerical simulation of fluid–structure–acoustic interaction motivated by healthy human phonation. *Journal of Computational and Applied Mathematics*, 472:116771, 2026.

[5] Harm Schutte. Aerodynamics of phonation. *Acta oto-rhino-laryngologica Belgica*, 40:344–57, 02 1986.

[6] Paul Maurerlehner, Stefan Schoder, Clemens Freidhager, Andreas Wurzinger, Alexander Hauser, Florian Kraxberger, Sebastian Falk, Stefan Kniesburges, Matthias Echternach, Michael Döllinger, and Manfred Kaltenbacher. Efficient numerical simulation of the human voice: simvoice – a three-dimensional simulation model based on a hybrid aeroacoustic approach. *e i Elektrotechnik und Informationstechnik*, 04 2021.

[7] Stefan Schoder and Manfred Kaltenbacher. Hybrid aeroacoustic computations: State of art and new achievements. *Journal of Theoretical and Computational Acoustics*, 27(4), December 2019.

[8] Stefan Schoder and Klaus Roppert. opencfs: Open source finite element software for coupled field simulation – part acoustics, 2025.

[9] Scott L. Thomson. Synthetic, self-oscillating vocal fold models for voice production research. *The Journal of the Acoustical Society of America*, 156(2):1283–1308, 08 2024.

[10] H. Gray and W.H. Lewis. *Anatomy of the Human Body*. Lea & Febiger, 1918.

[11] I.R. Titze. *Principles of Voice Production*. Prentice Hall, 1994.

[12] Camille Finck and Lionel Lejeune. Chapter 10.2 - structure and oscillatory function of the vocal folds. In Stefan M. Brudzynski, editor, *Handbook of Mammalian Vocalization*, volume 19 of *Handbook of Behavioral Neuroscience*, pages 427–438. Elsevier, 2010.

[13] Jack Jiang, Timothy O'Mara, David Conley, and David Hanson. Phonation threshold pressure measurements during phonation by airflow. *The Laryngoscope*, 109:425–32, 04 1999.

[14] Jorge Lucero. Dynamics of the vocal fold oscillation. *TEMA. Tendências em Matemática Aplicada e Computacional*, 6, 03 2005.

[15] Johannes Fischer, Paula L. Jordan, Fiona Stritt, Bernhard Richter, Louisa Traser, and Michael Bock. Dynamic 3d mri for vocal fold oscillation measurements. *Zeitschrift für Medizinische Physik*, 2026.

[16] Ingo Titze. Nonlinear source-filter coupling in phonation: Theory. *The Journal of the Acoustical Society of America*, 123:2733–49, 06 2008.

[17] Julian Chen. *Elements of Human Voice*. 08 2016.

[18] Bastian E. Rapp. Chapter 9 - fluids. In Bastian E. Rapp, editor, *Microfluidics: Modelling, Mechanics and Mathematics*, Micro and Nano Technologies, pages 243–263. Elsevier, Oxford, 2017.

[19] Franz Durst. *Grundgleichungen der Strömungsmechanik*, pages 123–164. Springer Berlin Heidelberg, Berlin, Heidelberg, 2006.

[20] Stefan Josef Schoder. *Aeroacoustic analogies based on compressible flow data*. PhD thesis, Technische Universität Wien, 2018.

[21] Manfred Kaltenbacher. *Computational Acoustics*. Springer Berlin Heidelberg, 2018.

[22] G. K. Batchelor. *An Introduction to Fluid Dynamics*. Cambridge Mathematical Library. Cambridge University Press, 2000.

[23] https://eaglepubs.erau.edu/introductiontoaerospaceflightvehicles/chapter/noise-of-flight-vehicles/. Accessed: 2026-05-20.

[24] Stefan J. Schoder, Clemens Junger, Michael Weitz, and Manfred Kaltenbacher. Conservative interpolation of aeroacoustic sources in a hybrid workflow applied to fan, 2020.

[25] Stefan Schoder, Paul Maurerlehner, Andreas Wurzinger, Alexander Hauser, Sebastian Falk, Stefan Kniesburges, Michael Döllinger, and Manfred Kaltenbacher. Aeroacoustic sound source characterization of the human voice production-perturbed convective wave equation. *Applied Sciences*, 11(6), 2021.

[26] Andreas Hüppe, Jens Grabinger, Manfred Kaltenbacher, Aaron Reppenhagen, Gerhard Dutzler, and Wolfram Kuehnel. A non-conforming finite element method for computational aeroacoustics in rotating systems. 06 2014.

[27] Michele De Gennaro, Helmut Kuehnelt, and Manfred Kaltenbacher. A numerical investigation of the laminar instability multi-tonal noise of aerofoils. 06 2012.

[28] Stefan Schoder and Klaus Roppert. opencfs-data: Data pre-post-processing tool for opencfs – aeroacoustics source filters, 02 2023.

[29] Stefan Schoder, Michael Weitz, Paul Maurerlehner, Alexander Hauser, Sebastian Falk, Stefan Kniesburges, Michael Döllinger, and Manfred Kaltenbacher. Hybrid aeroacoustic approach for the efficient numerical simulation of human phonation. *The Journal of the Acoustical Society of America*, 147:1179–1194, 02 2020.

[30] Michael James Lighthill. On sound generated aerodynamically i. general theory. *Proceedings of the Royal Society of London. A. Mathematical and Physical Sciences*, 211(1107):564–587, 03 1952.

[31] Tinghui Zheng, Sk Tang, and Wen Zhong Shen. Simulation of vortex sound using the viscous/acoustic splitting approach. *Transactions of the Canadian Society for Mechanical Engineering*, 35, 03 2011.

[32] Michael James Lighthill. On sound generated aerodynamically ii. turbulence as a source of sound. *Proceedings of the Royal Society of London. A. Mathematical and Physical Sciences*, 222(1148):1–32, 02 1954.

[33] N. Curle. The influence of solid boundaries upon aerodynamic sound. *Proceedings of the Royal Society of London. Series A, Mathematical and Physical Sciences*, 231(1187):505–514, 1955.

[34] B. F. Williams and D. L. Hawkings. Sound generation by turbulence and surfaces in arbitrary motion. *Philosophical Transactions of the Royal Society of London. Series A, Mathematical and Physical Sciences*, 264:321 – 342, 1969.

[35] Nicholas Oettle and David Sims-Williams. Automotive aeroacoustics: An overview. *Proceedings of the Institution of Mechanical Engineers, Part D: Journal of Automobile Engineering*, 231:095440701769514, 04 2017.

[36] M. S. Howe. Contributions to the theory of aerodynamic sound, with application to excess jet noise and the theory of the flute. *Journal of Fluid Mechanics*, 71(4):625–673, 1975.

[37] Andreas Wurzinger. *Development of a Validated Simulation Model for the Prevention of Flow-Induced Noise in Prostheses*. Phd thesis, 2026. Creators.

[38] Wolfgang Nagel, Michael Resch, Willi Jäger, Q. Zhang, Phong Bui, W.A. El-Askary, Matthias Meinke, and Wolfgang Schröder. *A Hybrid LES/CAA Method for Aeroacoustic Applications*. 01 2006.

[39] Tim Colonius, Sanjiva K Lele, and Parviz Moin. Sound generation in a mixing layer. *Journal of Fluid Mechanics*, 330:375–409, 1997.

[40] X. Gloerfelt, C. Bailly, and D. Juvé. Direct computation of the noise radiated by a subsonic cavity flow and application of integral methods. *Journal of Sound and Vibration*, 266(1):119–146, 2003.

[41] Olivier Marsden, Xavier Gloerfelt, and Christophe Bailly. Direct noise computation of adaptive control applied to a cavity flow. *Comptes Rendus Mecanique*, 331(6):423–429, 2003.

[42] Andrea Beck and Claus-Dieter Munz. Direct aeroacoustic simulations based on high order discontinuous galerkin schemes. In *Computational acoustics*, pages 159–204. Springer, 2017.

[43] Sauro Succi. *The Lattice Boltzmann Equation for Fluid Dynamics and Beyond*. Oxford University Press, Oxford, UK, 2001.

[44] G. Thömmes, Mohammed Seaid, and Mapundi Banda. Lattice boltzmann methods for shallow water flow applications. *International Journal for Numerical Methods in Fluids*, 55:673 – 692, 11 2007.

[45] S. S. Chikatamarla, C. E. Frouzakis, I. V. Karlin, A. G. Tomboulides, and K. B. Boulouchos. Lattice boltzmann method for direct numerical simulation of turbulent flows. *Journal of Fluid Mechanics*, 656:298–308, 2010.

[46] Manfred Krafczyk, Konstantin Kutscher, Ying Wang, and Martin Geier. Dns/les studies of turbulent flows based on the cumulant lattice boltzmann approach. pages 519–532, 12 2015.

[47] Ruddy Brionnaud, Miguel Chávez-Modena, Giuseppe Trapani, and David Holman. Direct noise computation with a lattice-boltzmann method and application to industrial test cases. 05 2016.

[48] J. C. Hardin and D. S. Pope. An acoustic/viscous splitting technique for computational aeroacoustics. *Theoretical and Computational Fluid Dynamics*, 6(5):323–340, 1994.

[49] Manfred Kaltenbacher. *Numerical Simulation of Mechatronic Sensors and Actuators*. Springer Berlin Heidelberg, 2015.

[50] Wen Zhong Shen and Jens Nørkær Sørensen. Aeroacoustic modelling of lowspeed flows. *Theoretical and Computational Fluid Dynamics*, 13:271–289, 1999.

[51] Jung Hee Seo and Young J. Moon. Perturbed compressible equations for aeroacoustic noise prediction at low mach numbers. *AIAA Journal*, 43:1716–1724, 2005.

[52] Jung H. Seo and Young J. Moon. Linearized perturbed compressible equations for low mach number aeroacoustics. *Journal of Computational Physics*, 218(2):702–719, 2006.

[53] R. Ewert and W. Schröder. Acoustic perturbation equations based on flow decomposition via source filtering. *Journal of Computational Physics*, 188(2):365–398, 2003.

[54] Fariborz Alipour, Christoph Brücker, Douglas Cook, Andreas Gommel, Manfred Kaltenbacher, Willy Mattheus, Luc Mongeau, Eric Nauman, Rüdiger Schwarze, Isao Tokuda, and Stefan Zorner. Mathematical models and numerical schemes for the simulation of human phonation. *Current Bioinformatics*, 6:323–343, 09 2011.

[55] Döllinger, Michael, Zhang, Zhaoyan, Schoder, Stefan, Sidlof, Petr, Tur, Bogac, and Kniesburges, Stefan. Overview on state-of-the-art numerical modeling of the phonation process. *Acta Acust.*, 7:25, 2023.

[56] James L. Flanagan and Lorinda L. Landgraf. Self-oscillating source for vocal-tract synthesizers. *IEEE Transactions on Audio and Electroacoustics*, 16:57–64, 1968.

[57] Edson Cataldo, Fabiana R. Leta, Jorge Lucero, and Lucas Nicolato. Synthesis of voiced sounds using low-dimensional models of the vocal cords and time-varying subglottal pressure. *Mechanics Research Communications*, 33(2):250–260, 2006.

[58] K. Ishizaka and J. L. Flanagan. Synthesis of voiced sounds from a two-mass model of the vocal cords. *The Bell System Technical Journal*, 51(6):1233–1268, 1972.

[59] Brad H. Story and Ingo R. Titze. Voice simulation with a body-cover model of the vocal folds. *The Journal of the Acoustical Society of America*, 97(2):1249–1260, 02 1995.

[60] Ingo Titze. The physics of small-amplitude oscillation of the vocal folds. *The Journal of the Acoustical Society of America*, 83:1536–52, 05 1988.

[61] Anxiong Yang, Jörg Lohscheller, David Berry, S. Becker, Ulrich Eysholdt, Daniel Voigt, and Michael Döllinger. Biomechanical modeling of the three-dimensional aspects of human vocal fold dynamics. *The Journal of the Acoustical Society of America*, 127:1014–31, 02 2010.

[62] Fariborz Alipour, David Berry, and Ingo Titze. A finite-element model of vocal-fold vibration. *The Journal of the Acoustical Society of America*, 108:3003–12, 12 2000.

[63] Marcelo de Oliveira Rosa, José Carlos Pereira, Marcos Grellet, and Abeer Alwan. A contribution to simulating a three-dimensional larynx model using the finite element method. *The Journal of the Acoustical Society of America*, 114 5:2893–905, 2003.

[64] R. C. Scherer, D. Shinwari, K. J. De Witt, C. Zhang, B. R. Kucinschi, and A. A. Afjeh. Intraglottal pressure profiles for a symmetric and oblique glottis with a divergence angle of 10 degrees. *The Journal of the Acoustical Society of America*, 109(4):1616–1630, 2001.

[65] Mihai Mihaescu, Sid M Khosla, Shanmugam Murugappan, and Ephraim J Gutmark. Unsteady laryngeal airflow simulations of the intra-glottal vortical structures. *The Journal of the Acoustical Society of America*, 127(1):435–444, 2010.

[66] Willy Mattheus and Christoph Brücker. Asymmetric glottal jet deflection: Differences of two- and three-dimensional models. *The Journal of the Acoustical Society of America*, 130:EL373–9, 12 2011.

[67] X. Zheng, R. Mittal, and S. Bielamowicz. A computational study of asymmetric glottal jet deflection during phonation. *The Journal of the Acoustical Society of America*, 129(4):2133–2143, 04 2011.

[68] Hossein Sadeghi, Stefan Kniesburges, Sebastian Falk, Manfred Kaltenbacher, Anne Schützenberger, and Michael Döllinger. Towards a clinically applicable computational larynx model. *Applied Sciences*, 9(11), 2019.

[69] S. Zörner, Petr Šidlof, A. Hüppe, and Manfred Kaltenbacher. Flow and acoustic effects in the larynx for varying geometries. *Acta Acustica united with Acustica*, 102:257–267, 03 2016.

[70] Petr Šidlof, Jaromír Horáček, and Václav Řidký. Parallel cfd simulation of flow in a 3d model of vibrating human vocal folds. *Computers Fluids*, 80:290–300, 2013. Selected contributions of the 23rd International Conference on Parallel Fluid Dynamics ParCFD2011.

[71] P. Šidlof, S. Zörner, and A. Hüppe. A hybrid approach to the computational aeroacoustics of human voice production. *Biomechanics and Modeling in Mechanobiology*, 14(3):473–488, 2015.

[72] Lukas Schickhofer and Mihai Mihaescu. Analysis of the aerodynamic sound of speech through static vocal tract models of various glottal shapes. *Journal of Biomechanics*, 99:109484, 11 2019.

[73] Martin Lasota, Petr Šidlof, Manfred Kaltenbacher, and Stefan Schoder. Impact of the sub-grid scale turbulence model in aeroacoustic simulation of human voice. *Applied Sciences*, 11(4), 2021.

[74] Martin Lasota, Petr Šidlof, Paul Maurerlehner, Manfred Kaltenbacher, and Stefan Schoder. Anisotropic minimum dissipation subgrid-scale model in hybrid aeroacoustic simulations of human phonation. *The Journal of the Acoustical Society of America*, 153(2):1052–1063, February 2023.

[75] Michael Döllinger, Thomas Braunschweig, Jörg Lohscheller, U Eysholdt, and Ulrich Hoppe. Normal voice production: Computation of driving parameters from endoscopic digital high speed images. *Methods of information in medicine*, 42:271–6, 02 2003.

[76] Paul J. Hadwin and Sean D. Peterson. An extended kalman filter approach to non-stationary bayesian estimation of reduced-order vocal fold model parameters. *The Journal of the Acoustical Society of America*, 141(4):2909–2920, 04 2017.

[77] Pablo Gómez, Anne Schützenberger, Marion Semmler, and Michael Döllinger. Laryngeal pressure estimation with a recurrent neural network. *IEEE Journal of Translational Engineering in Health and Medicine*, PP:1–1, 12 2018.

[78] Yang Zhang, Weili Jiang, Luning Sun, Jian-Xun Wang, Simeon Smith, Ingo Titze, Xudong Zheng, and Qian Xue. A deep-learning based generalized reduced-order model of glottal flow during normal phonation, 05 2020.

[79] Yang Zhang, Pu Tianmei, Chunhua Zhou, and Hongming Cai. An improved glottal flow model based on seq2seq lstm for simulation of vocal fold vibration. *Journal of Voice*, 05 2022.

[80] Zhaoyan Zhang. Estimation of vocal fold physiology from voice acoustics using machine learning. *The Journal of the Acoustical Society of America*, 147:EL264–EL270, 03 2020.

[81] Zhaoyan Zhang. Voice feature selection to improve performance of machine learning models for voice production inversion. *Journal of Voice*, 37, 04 2021.

[82] Zhaoyan Zhang. Estimating subglottal pressure and vocal fold adduction from the produced voice in a single-subject study (l). *The Journal of the Acoustical Society of America*, 151:1337–1340, 02 2022.

[83] Andreas Wurzinger, Patrick Heidegger, and Stefan Schoder. pycfs-data: Data processing framework in python for opencfs, 2026.

[84] Christopher Greenshields and Henry Weller. *Notes on Computational Fluid Dynamics: General Principles*. CFD Direct Ltd, Reading, UK, 2022.

[85] Gergely Kristóf. *Áramlások numerikus modellezése*. Akadémiai Kiadó, 2019.

[86] Sebastian Falk, Stefan Kniesburges, Stefan Schoder, Bernhard Jakubaß, Paul Maurerlehner, Matthias Echternach, Manfred Kaltenbacher, and Michael Döllinger. 3d-fv-fe aeroacoustic larynx model for investigation of functional based voice disorders. *Frontiers in Physiology*, Volume 12 - 2021, 2021.

[87] Brad Story, Ingo Titze, and Eric Hoffman. Vocal tract area functions from magnetic resonance imaging. *The Journal of the Acoustical Society of America*, 100:537–54, 08 1996.